



FP7-600716

Whole-Body Compliant Dynamical Contacts in Cognitive Humanoids

D2.2

Models of human whole body motions in contact with rigid and compliant support surfaces

Editor(s)	Morteza Azad ¹ , Michael Mistry ¹ and Jan Babič ²
Responsible Partner	JSI
Affiliations	¹ School of Computer Science, University of Birmingham, UK. ² Department for Automation, Biocybernetics and Robotics, Jožef Stefan Institute, Ljubljana, Slovenia.
Status-Version:	Final-1.0
Date:	29/2/2016
EC Distribution:	Consortium
Project Number:	600716
Project Title:	Whole-Body Compliant Dynamical Contacts in Cognitive Humanoids

Title of Deliverable:	Models of human whole body motions in contact with rigid and compliant support surfaces
Date of delivery to the EC:	29/2/2016

Workpackage responsible for the Deliverable	WP2
Editor(s):	Morteza Azad, Michael Mistry and Jan Babič
Contributor(s):	Morteza Azad (UB), Michael Mistry (UB), Chie Takahashi (UB), Elmar Rueckert (TUD), Jan Peters (TUD), Jernej Čamernik (JSI), Jan Babič (JSI)
Reviewer(s):	
Approved by:	All Partners
Abstract	The scope of the current deliverable is to present the results on developing models of human whole body motions in contact with environment.
Keyword List:	contacts, model learning, probabilistic movement representations

Document Revision History

Version	Date	Description	Author
v. 1.0	29 Feb 2016	Final Version	Morteza Azad

Table of Contents

1	Introduction	5
2	Manipulability of the Center of Mass: A Tool to Study, Analyse and Measure the Ability to Balance	6
2.1	Introduction	6
2.2	Kinematic Manipulability of The CoM	8
2.3	Dynamic Manipulability of the CoM: From Impulsive Dynamics	10
2.3.1	Change-of-velocity Ellipsoid—Unit Joint Impulse	11
2.3.2	Change-of-velocity Ellipsoid—Unit Joint Velocity	12
2.4	Application to Design and Analysis	13
2.4.1	Joint Limits	14
2.5	Experiments on Humans	14
2.5.1	Methods	14
2.5.2	Model	17
2.5.3	Results	18
2.6	Conclusion	19
3	Postural Control Precedes and Predicts Volitional Motor Control	21
3.1	Introduction	21
3.2	Results	22
3.2.1	Subjects chose task dependent contact locations	23
3.2.2	Supportive and goal-directed movements synchronize	24
3.2.3	Modeling joint distributions over limb trajectories	24
3.2.4	Supportive contacts predict goal-directed movements	26
3.2.5	Trunk adaptation precedes arm adaptation	27
3.3	Discussion	29
3.3.1	A pre-test for central nervous system disorders affecting postural control	29
3.3.2	Evidence for learning on multiple time scales	30
3.3.3	A robot controller that actively seeks for contacts	30
3.4	Methods	31
3.4.1	Participants	31
3.4.2	Apparatus	31
3.4.3	Coordinate frames	31
3.4.4	Procedure	32
3.4.5	Data processing	32

3.4.6	Statistical tests	32
3.4.7	Computing predictions through conditioning	33
3.4.8	Phase modulated probabilistic models of trajectories	33
3.4.9	Computing predictions in trajectories	35
3.4.10	Computing model comparisons in trajectories	35
3.4.11	Computing task likelihoods in trajectories	36
3.5	Supporting Information	36
4	Use of rigid contacts during continuous perturbations	40
1	Introduction	40
2	Methods	41
2.1	Experimental protocol	41
2.2	Data analysis	42
2.3	Statistical analysis	42
3	Results	43
4	Conclusions	49
5	Learning compliant contacts	51
1	Introduction	51
2	Methods	52
2.1	Modelling	52
2.2	Experimental Design	52
2.3	Apparatus and Stimuli	52
2.4	Procedure and analyses	54
3	Results and Discussions	55
3.1	Participants	55
3.2	Ongoing Results	55
3.3	Brief Discussion	55

Chapter 1

Introduction

This deliverable summarizes the contribution of the CoDyCo consortium in tasks T2.2 and T2.3 at the end of the third year. These tasks are *design of models for human whole body motion in contact*, and *strategies of dealing with uncertainties in contact*, respectively. The results are briefly explained in four chapters. In chapter 2, dynamic manipulability of the centre of mass (CoM) is introduced as a metric for measuring the balance ability of legged robots while they are in contact with their environment. Experiments on human subjects show the applicability of this theory in analysing balancing recovery motion in humans. Chapter 3 investigates the use of supporting contact (and its relationship with task) while it is required for accomplishing a task. In the experiments, human subjects are asked to reach a target by the motion of one arm while they has to maintain their postural balance with the other arm. In a novel movement model, strong correlations between both arms are found which were used to predict the reaching motion solely from observing the motion related to keeping postural stability. This finding has the potential to impact pre-tests of central nervous system disorders that are less prone to factors like stress, sleep deprivation and age compared to the classical cognitive tests. In robotics, the model can be exploited to overcome current limitations of autonomous robots in interacting with the environment through supportive contacts. In chapter 4, the effects of using handles is studied for posture control of standing subjects while they are perturbed by external forces. It is shown that the use of handles significantly reduces the displacement of the centre of pressure. Also, it is observed that subjects clearly relied on using the handle for support, even though the perturbations did not pose a significant balance threat. Chapter 5 is a report of pilot study on learning compliant contacts by human subjects. Subjects are asked to push a compliant surface to a certain target in order to learn the parameters of the contact. The compliant surface is realized by using a haptic device. Then, in a trial experiment, the performance of the subjects is analysed in reaching a new target position in terms of the time needed to reach that target.

Chapter 2

Manipulability of the Center of Mass: A Tool to Study, Analyse and Measure the Ability to Balance

This chapter introduces a set of metrics to study, analyse and measure the ability to balance for both humans and legged robots. This set of metrics, which we call manipulability of the center of mass, are defined based on the concept of end-effector manipulability in the literature. Regarding the center of mass as an end-effector and using impulsive dynamics, the metrics are calculated to study the ability to move and accelerate this point. They graphically show the instantaneous change of the center of mass velocity due to the unit weighted norm of instantaneous changes of the joint velocities or impulses at the joints. The proposed metrics can be computed for humans and general legged robots with floating base and multiple contacts with the environment in 3D space. This chapter also provides the results of experiments on humans to verify the application of the metrics. In the experiments, the centers of mass of human subjects in different configurations are perturbed and joint torques are computed by using inverse dynamics. The metrics are shown to be suitable for comparing different postures in the sense of the total required effort for balance maintenance.

2.1 Introduction

Humans and legged robots operate in and interact with unstructured and unpredictable environment. The key to their safe operation is their ability to maintain postural stability in various body configurations. To this end, there has been a considerable research effort in biomechanics and neuroscience to study and understand human postural control. Some studies investigated the postural control in bipedal stance or walking [39, 55, 86]. Other studies focused on effects of using additional supportive contacts to the stability [8, 53].

In robotics many balance criteria have been proposed over the last years in order to help to design balancing controllers. Among them, zero moment point (ZMP) [82, 83] or center of pressure (CoP), foot rotation indicator (FRI) [34] and zero rate of change of angular momentum (ZRAM) [35] are the most famous and applicable ones. Unfortunately, most of the above mentioned criteria are not well-defined when the robot has multiple non-planar

contacts with its environment [35]. The other problem with these criteria is that none of them is able to distinguish between different balanced configurations of a robot in terms of the ability to keep the balance. In other words, all balanced configurations for a robot are assumed to be the same as long as they meet the balance criteria. Here, we tackle this problem and introduce a set of metrics that quantitatively evaluate the ability to balance in different postural and contact configurations. These metrics, which are defined for both humans and robots, can also be applicable in comparing different configurations in the sense of balance ability.

As the center of mass (CoM) plays a key role in a balancing motion, the ability to balance, in both humans and robots, depends on the ability to move and accelerate the CoM. To define a set of proper metrics, we regard the CoM as an end-effector and employ the basic concept of end-effector manipulability in the literature [24] and calculate a set of metrics which are called manipulability of the CoM. They measure the ability to accelerate the CoM with the constant weighted norm of joint change of velocities or impulses at the joints.

Unlike the end-effector manipulability which is a quite developed topic [15, 24, 37, 62, 90], there have not been many studies on CoM manipulability in the literature. Naksuk and Lee [58] introduced ZMP manipulability as an extension to the ZMP balance criterion based on the concept of dynamic manipulability of end-effectors. Then, Cotton *et al.* [18] were the first to introduce dynamic manipulability of the CoM for humanoid robots. They used the motion equation of the robot to calculate the acceleration of the CoM due to available torque at the joints. Recently, Gu *et al.* [36] proposed feasible CoM dynamic manipulability (FCDM) for planar humanoids. To evaluate the feasibility of the manipulability index, they considered the ground-contact force constraints such as friction cone and unilaterality of the normal force. However, their proposed method is not developed for floating base robots with multiple contacts.

In this chapter, we employ a different method for calculating the manipulability of the CoM. In this method, we do not work out the relationship between joint torques and acceleration of the CoM by using motion equations. Instead, we apply impulses at the actuated joints and then compute the relationship between the impulses (or instantaneous changes at the joint velocities due to the impulses) and the instantaneous change of the CoM velocity. This is in fact the method that is used by Featherstone [28, 29] to study the balance ability of robots on a single point. This approach allows us to derive a set of configuration based metrics (i.e. velocity independent) which are applicable to all types of legged (floating base) robots and also humans with different contact conditions. Therefore, these metrics provide a tool to study balancing motions in humans and robots and also design better and more efficient robots in the future.

In the calculation of the CoM manipulability, we take into account the effects of inertial parameters as well as under-actuation and kinematics constraints. The under-actuation is due to the floating base and kinematic constraints are due to multiple contacts with the environment, such as hands and feet for biped robots or humans. As a result of the manipulability analysis, we obtain two types of ellipsoids which graphically show 1) instantaneous change of the CoM velocity due to the weighted unit norm of impulses at the actuated joints, and 2) instantaneous change of the CoM velocity due to the weighted unit norm of instantaneous changes of joint velocities. These ellipsoids, which are calculated by using impulsive dynamics, take into account the ability to cause the motion at the CoM. The first type of ellipsoid shows

how a certain amount of torque at the joints can accelerate the CoM. This can be used to study the efficiency in the sense of required torque. The second ellipsoid shows the ability to move the CoM with a certain amount of movement at the joints. This ability can be considered as maneuverability for a human or a robot: the higher the maneuverability (larger ellipsoid), the less movement is required to correct the position of the CoM.

In order to investigate the applicability of the proposed metrics for human studies, we perform experiments on human subjects. We study the balance recovery motions of eleven subjects in five different configurations and compare the total amount of torque that is done by the subjects to maintain balance at each configuration. We apply controlled forces to the CoM of the subjects to provide same perturbations at the CoM in all configurations. Then, by using inverse dynamics, we compute the average total joint torques that is applied by the subjects at each configuration. This allows us to rank the configurations in terms of required torque for humans to keep their balance. It is shown in the experimental results (section 2.5) that our proposed metric for torque efficiency predicts the same ranking for the selected configurations. This illustrates that the manipulability of the CoM is a suitable tool for studying balance in humans as well as robots.

2.2 Kinematic Manipulability of The CoM

The concept of manipulability (of end-effectors) for manipulators, first introduced by Yoshikawa [?]. He proposed that $\sqrt{\mathbf{J}_e \mathbf{J}_e^T}$, where \mathbf{J}_e is the Jacobian of end-effector, can be used to measure the capability of a manipulator in a specific configuration. He also extended this metric to dynamic manipulability by including the dynamics equations of manipulators [90]. However, Doty *et. al.* [24] pointed out that $\sqrt{\mathbf{J}_e \mathbf{J}_e^T}$ have no physical meaning when dealing with general robots with a combination of different joint types (e.g. revolute and prismatic joints). They proposed to use a weighting matrix to solve this issue and make consistency in the units.

To extend the manipulability concept to be used for CoM of legged robots, we need to regard the CoM as an end-effector, and also include floating-base dynamics and kinematic constraints (due to multiple contacts with the environment) in the equations. Let $\mathbf{q} \in \mathbb{R}^n$ denote the vector of generalized coordinates of a robot which has 6 virtual unactuated degrees of freedom (DoF) due to its floating base. Assume that there are l linearly independent kinematic constraints acting on the robot. Therefore,

$$\mathbf{J}_c \dot{\mathbf{q}} = \mathbf{0}, \quad (2.1)$$

where $\mathbf{J}_c \in \mathbb{R}^{l \times n}$ is the Jacobian of the constraints. By defining a projector $\mathbf{P} = \mathbf{I} - \mathbf{J}_c^\# \mathbf{J}_c$, we can project any arbitrary vector $\mathbf{v} \in \mathbb{R}^n$ from the joint velocity space into the null space of the constraints as

$$\dot{\mathbf{q}} = \mathbf{P} \mathbf{v}. \quad (2.2)$$

Note that $\mathbf{I} \in \mathbb{R}^{n \times n}$ is an identity matrix and superscript $\#$ indicates the weighted generalized inverse as introduced in [23]. Since \mathbf{J}_c is full row rank, $\mathbf{J}_c^\#$ is

$$\mathbf{J}_c^\# = \mathbf{W}_q^{-1} \mathbf{J}_c^T (\mathbf{J}_c \mathbf{W}_q^{-1} \mathbf{J}_c^T)^{-1}. \quad (2.3)$$

Also, the followings are two useful properties of \mathbf{P} which can be concluded from its definition:

$$1. \quad \mathbf{P}^2 = \mathbf{P}$$

$$2. \quad \mathbf{P}^T = \mathbf{W}_q \mathbf{P} \mathbf{W}_q^{-1}$$

Now, to calculate the kinematic manipulability of the CoM, we consider a unit weighted sphere of joint velocities as

$$\dot{\mathbf{q}}^T \mathbf{W}_q \dot{\mathbf{q}} = 1, \quad (2.4)$$

where \mathbf{W}_q is a symmetric positive definite matrix and is used in (2.4) to provide consistency in units. In the case that all joints are revolute joints and the robot has a fixed base, one can set \mathbf{W}_q to identity. Also one physically meaningful option for this metric is the joint-space inertia matrix which makes (2.4) equal to the double of the kinetic energy (the kinetic energy would be $1/2$ in this case).

By replacing (2.2) into (2.4), we have

$$\mathbf{v}^T \mathbf{P}^T \mathbf{W}_q \mathbf{P} \mathbf{v} = 1. \quad (2.5)$$

Let $\mathbf{c} \in \mathbb{R}^3$ and $\mathbf{J} \in \mathbb{R}^{3 \times n}$ denote the position and Jacobian of the CoM [76] in the world frame, respectively. Then, the velocity of the CoM will be

$$\dot{\mathbf{c}} = \mathbf{J} \dot{\mathbf{q}} = \mathbf{J} \mathbf{P} \mathbf{v} = \mathbf{J}_p \mathbf{v}, \quad (2.6)$$

where $\mathbf{J}_p \in \mathbb{R}^{3 \times n}$ can be regarded as the Jacobian of the CoM in the constrained space. Here, we assume that there is no constraint on the movement of the CoM and therefore \mathbf{J}_p is full row rank. In case that there are any constraints on the CoM, one can define a new coordinate frame with axes aligned with the constraints and express $\dot{\mathbf{c}}$ and \mathbf{J}_p in the new frame. So the Jacobian in the new frame will be full row rank but it will have a lower dimension than \mathbf{J}_p .

Since \mathbf{J}_p is full row rank, we can write its weighted generalized inverse as

$$\mathbf{J}_p^\# = \mathbf{W}_q^{-1} \mathbf{J}_p^T (\mathbf{J}_p \mathbf{W}_q^{-1} \mathbf{J}_p^T)^{-1}. \quad (2.7)$$

So, by using the definition of weighted generalized inverses in [23], we can conclude from (2.6) that

$$\mathbf{v} = \mathbf{J}_p^\# \dot{\mathbf{c}} + \mathbf{N} \mathbf{v}_0, \quad (2.8)$$

where $\mathbf{v}_0 \in \mathbb{R}^n$ is an arbitrary vector and $\mathbf{N} = \mathbf{I} - \mathbf{J}_p^\# \mathbf{J}_p$ is a projector to the null space of \mathbf{J}_p .

Now, by replacing (2.8) into (2.5) we will have

$$\begin{aligned} 1 &= \dot{\mathbf{c}}^T \mathbf{J}_p^{\#T} \mathbf{P}^T \mathbf{W}_q \mathbf{P} \mathbf{J}_p^\# \dot{\mathbf{c}} + \dot{\mathbf{c}}^T \mathbf{J}_p^{\#T} \mathbf{P}^T \mathbf{W}_q \mathbf{P} \mathbf{N} \mathbf{v}_0 \\ &\quad + \mathbf{v}_0^T \mathbf{N}^T \mathbf{P}^T \mathbf{W}_q \mathbf{P} \mathbf{J}_p^\# \dot{\mathbf{c}} + \mathbf{v}_0^T \mathbf{N}^T \mathbf{P}^T \mathbf{W}_q \mathbf{P} \mathbf{N} \mathbf{v}_0 \\ &= \dot{\mathbf{c}}^T \mathbf{J}_p^{\#T} \mathbf{P}^T \mathbf{W}_q \mathbf{P} \mathbf{J}_p^\# \dot{\mathbf{c}} + \mathbf{v}_0^T \mathbf{N}^T \mathbf{P}^T \mathbf{W}_q \mathbf{P} \mathbf{N} \mathbf{v}_0 \end{aligned} \quad (2.9)$$

Note that $\mathbf{J}_p^{\#T} \mathbf{P}^T \mathbf{W}_q \mathbf{P} \mathbf{N} = \mathbf{N}^T \mathbf{P}^T \mathbf{W}_q \mathbf{P} \mathbf{J}_p^\# = \mathbf{0}$. This can be proved by using (2.7) and also the definition of \mathbf{N} . Since both terms in the right hand side of (2.9) are positive, we can conclude that

$$0 \leq \dot{\mathbf{c}}^T \mathbf{J}_p^{\#T} \mathbf{P}^T \mathbf{W}_q \mathbf{P} \mathbf{J}_p^\# \dot{\mathbf{c}} \leq 1. \quad (2.10)$$

By using the properties of \mathbf{P} , which are mentioned earlier in this section, and also knowing that $\mathbf{J}_p \mathbf{P} = \mathbf{J}_p$, the above equation is simplified to

$$0 \leq \dot{\mathbf{c}}^T (\mathbf{J} \mathbf{P} \mathbf{W}_q^{-1} \mathbf{J}^T)^{-1} \dot{\mathbf{c}} \leq 1. \quad (2.11)$$

Equation (2.11) defines an ellipsoid in the velocity space at the CoM of the robot. The principal axes and radii of this ellipsoid are the eigenvectors and eigenvalues of matrix $\mathbf{JPW}_q^{-1}\mathbf{J}^T$, respectively. The velocity ellipsoid represents the robot's kinematic ability to move the CoM in different directions, without considering whether or not the robot is capable of causing such motions via its actuators. The reason is that, this analysis is in the velocity level and therefore the motion equations are not involved.

2.3 Dynamic Manipulability of the CoM: From Impulsive Dynamics

In this section, we use impulsive dynamics to study the manipulability of the CoM. Therefore, unlike section 2.2, this section provides an impulse-based analysis that enables us to investigate the manipulability of the CoM at the acceleration level by involving the motion equations into the calculations. As a result of this analysis, we define two types of ellipsoids which we call them *change-of-velocity ellipsoids* in this paper. The first type shows the effects of the unit weighted impulses at the joints on the change of the CoM velocity. The second one shows the change of the CoM velocity due to the unit norm of instantaneous changes in joint velocities (due to non-zero impulses at the actuated joints). The former is called *unit joint impulse* and the latter is called *unit joint velocity* in this paper. As already mentioned, these ellipsoids can be used to study energy efficiency and maneuverability, respectively.

Consider the motion equations of a floating-base robot as

$$\mathbf{M}(\mathbf{q})\ddot{\mathbf{q}} + \mathbf{h}(\mathbf{q}, \dot{\mathbf{q}}) + \mathbf{g}(\mathbf{q}) = \mathbf{B}\boldsymbol{\tau} + \mathbf{J}_c^T(\mathbf{q})\mathbf{f}_c, \quad (2.12)$$

where $\mathbf{M} \in \mathbb{R}^{n \times n}$ is the joint-space inertia matrix, $\mathbf{h} \in \mathbb{R}^n$ is the vector of centripetal and Coriolis forces, $\mathbf{g} \in \mathbb{R}^n$ is the vector of gravity force, $\mathbf{B} \in \mathbb{R}^{n \times k}$ is the selection matrix for the actuated joints, $\boldsymbol{\tau} \in \mathbb{R}^k$ is the vector of actuated joint torques and $\mathbf{f}_c \in \mathbb{R}^l$ is the vector of the constraint forces. The kinematic constraints are either due to the kinematic loops in the mechanism or contacts with the environment (assuming that there is no sliding or loss of contact). The latter models the hands and feet contacts for a humanoid or a legged robot.

According to impulsive dynamics (§11.7 in [27]), the impulsive equation of motion for a general robot, concluded from (2.12), is

$$\mathbf{M} \Delta \dot{\mathbf{q}} = \mathbf{B}\boldsymbol{\tau}' + \boldsymbol{\tau}'_c, \quad (2.13)$$

where $\boldsymbol{\tau}'$ is the impulse at the actuated joints, $\boldsymbol{\tau}'_c = \mathbf{J}_c^T \mathbf{f}'_c$ is the impulse due to the contact forces (via kinematic constraints), \mathbf{f}'_c is the impulse of the contact forces and $\Delta \dot{\mathbf{q}}$ is instantaneous changes of joint velocities.

We solve (2.13) for $\Delta \dot{\mathbf{q}}$ and obtain

$$\Delta \dot{\mathbf{q}} = \mathbf{M}^{-1} \mathbf{B} \boldsymbol{\tau}' + \mathbf{M}^{-1} \mathbf{J}_c^T \mathbf{f}'_c. \quad (2.14)$$

It is known that $\mathbf{J}_c \Delta \dot{\mathbf{q}} = \mathbf{0}$, due to the kinematic constraints. Hence,

$$\mathbf{J}_c \Delta \dot{\mathbf{q}} = \mathbf{J}_c \mathbf{M}^{-1} \mathbf{B} \boldsymbol{\tau}' + \mathbf{J}_c \mathbf{M}^{-1} \mathbf{J}_c^T \mathbf{f}'_c = \mathbf{0}. \quad (2.15)$$

Since \mathbf{J}_c is full row rank, $\mathbf{J}_c \mathbf{M}^{-1} \mathbf{J}_c^T$ is invertible. Therefore,

$$\mathbf{f}'_c = -(\mathbf{J}_c \mathbf{M}^{-1} \mathbf{J}_c^T)^{-1} \mathbf{J}_c \mathbf{M}^{-1} \mathbf{B} \boldsymbol{\tau}'. \quad (2.16)$$

By substituting (2.16) into (2.14), we obtain

$$\Delta \dot{\mathbf{q}} = \mathbf{P}_M \mathbf{M}^{-1} \mathbf{B} \boldsymbol{\tau}', \quad (2.17)$$

where

$$\mathbf{P}_M = \mathbf{I} - \mathbf{J}_{c_M}^\# \mathbf{J}_c, \quad (2.18)$$

and

$$\mathbf{J}_{c_M}^\# = \mathbf{M}^{-1} \mathbf{J}_c^T (\mathbf{J}_c \mathbf{M}^{-1} \mathbf{J}_c^T)^{-1}, \quad (2.19)$$

is a generalized inverse of \mathbf{J}_c with the joint-space inertia matrix as the weighting matrix. So,

$$\Delta \dot{\mathbf{c}} = \mathbf{J} \Delta \dot{\mathbf{q}} = \mathbf{J} \mathbf{P}_M \mathbf{M}^{-1} \mathbf{B} \boldsymbol{\tau}' = \mathbf{J}_\tau \boldsymbol{\tau}', \quad (2.20)$$

where

$$\mathbf{J}_\tau = \mathbf{J} \mathbf{P}_M \mathbf{M}^{-1} \mathbf{B}, \quad (2.21)$$

and $\Delta \dot{\mathbf{c}}$ is the instantaneous change of the CoM velocity. Matrix \mathbf{J}_τ can be regarded as a Jacobian that maps the impulse $\boldsymbol{\tau}'$ to the step change at the CoM velocity. In this paper, we assume that this matrix is full row rank, implying that the CoM is not constrained and is controllable in all directions. In case that this assumption is not valid, one can define a new coordinate frame with the axes aligned with the constraints and uncontrollable directions of the CoM and express $\Delta \dot{\mathbf{c}}$ and \mathbf{J}_τ in the new frame. So the Jacobian in the new frame will be full row rank in a lower dimension.

2.3.1 Change-of-velocity Ellipsoid—Unit Joint Impulse

In this subsection, we calculate the relationship between instantaneous change of the CoM velocity and the unit weighted norm of impulse at the actuated joints. Since the actuated joints are not restricted to be the same type or strength, we define a metric \mathbf{W}_τ to unify the units and strengths of $\boldsymbol{\tau}'$ in

$$\boldsymbol{\tau}'^T \mathbf{W}_\tau \boldsymbol{\tau}' = 1, \quad (2.22)$$

where \mathbf{W}_τ is a weighting matrix. According to (2.20), we can write

$$\boldsymbol{\tau}' = \mathbf{J}_\tau^\# \Delta \dot{\mathbf{c}} + \mathbf{N}_\tau \boldsymbol{\tau}'_0, \quad (2.23)$$

where $\mathbf{N}_\tau = \mathbf{I} - \mathbf{J}_\tau^\# \mathbf{J}_\tau$ and

$$\mathbf{J}_\tau^\# = \mathbf{W}_\tau^{-1} \mathbf{J}_\tau^T (\mathbf{J}_\tau \mathbf{W}_\tau^{-1} \mathbf{J}_\tau^T)^{-1}. \quad (2.24)$$

Thus, by replacing (2.23) into (2.22), we will have

$$\begin{aligned} 1 &= (\mathbf{J}_\tau^\# \Delta \dot{\mathbf{c}} + \mathbf{N}_\tau \boldsymbol{\tau}'_0)^T \mathbf{W}_\tau (\mathbf{J}_\tau^\# \Delta \dot{\mathbf{c}} + \mathbf{N}_\tau \boldsymbol{\tau}'_0) \\ &= \Delta \dot{\mathbf{c}}^T \mathbf{J}_\tau^{\#T} \mathbf{W}_\tau \mathbf{J}_\tau^\# \Delta \dot{\mathbf{c}} + \Delta \dot{\mathbf{c}}^T \mathbf{J}_\tau^{\#T} \mathbf{W}_\tau \mathbf{N}_\tau \boldsymbol{\tau}'_0 \\ &\quad + \boldsymbol{\tau}'_0^T \mathbf{N}_\tau^T \mathbf{W}_\tau \mathbf{J}_\tau^\# \Delta \dot{\mathbf{c}} + \boldsymbol{\tau}'_0^T \mathbf{N}_\tau^T \mathbf{W}_\tau \mathbf{N}_\tau \boldsymbol{\tau}'_0 \\ &= \Delta \dot{\mathbf{c}}^T \mathbf{J}_\tau^{\#T} \mathbf{W}_\tau \mathbf{J}_\tau^\# \Delta \dot{\mathbf{c}} + \boldsymbol{\tau}'_0^T \mathbf{N}_\tau^T \mathbf{W}_\tau \mathbf{N}_\tau \boldsymbol{\tau}'_0 \end{aligned} \quad (2.25)$$

Note that $\Delta\dot{\mathbf{c}}^T \mathbf{J}_\tau^{\#T} \mathbf{W}_\tau \mathbf{N}_\tau \boldsymbol{\tau}'_0 = \boldsymbol{\tau}'_0^T \mathbf{N}_\tau^T \mathbf{W}_\tau \mathbf{J}_\tau^{\#} \Delta\dot{\mathbf{c}} = 0$. Hence,

$$0 \leq \Delta\dot{\mathbf{c}}^T \mathbf{J}_\tau^{\#T} \mathbf{W}_\tau \mathbf{J}_\tau^{\#} \Delta\dot{\mathbf{c}} \leq 1 \quad (2.26)$$

and therefore

$$0 \leq \Delta\dot{\mathbf{c}}^T (\mathbf{J}_\tau \mathbf{W}_\tau^{-1} \mathbf{J}_\tau^T)^{-1} \Delta\dot{\mathbf{c}} \leq 1. \quad (2.27)$$

The above equation defines an ellipsoid in the acceleration space which represents instantaneous change of the velocity of the CoM due to the unit weighted sphere of impulses at the actuated joints. This ellipsoid is characterized by the eigenvectors and eigenvalues of matrix $\mathbf{J}_\tau \mathbf{W}_\tau^{-1} \mathbf{J}_\tau^T$. According to (2.27), this ellipsoid captures the effect of both under-actuation (due to the floating base) and kinematic constraints (due to the contacts) in the relationship between instantaneous change of the CoM velocity and impulses at the joints. Therefore, it is claimed to be a proper tool to study energy efficiency in balancing motions. We verify this claim in the next section by performing experiments on humans.

2.3.2 Change-of-velocity Ellipsoid—Unit Joint Velocity

Here, we calculate instantaneous change of the CoM velocity due to the unit weighted norm of instantaneous changes of joint velocities. First, we consider same equation as (2.4) for instantaneous changes of joint velocities as

$$\Delta\dot{\mathbf{q}}^T \mathbf{W}_q \Delta\dot{\mathbf{q}} = 1. \quad (2.28)$$

Before substituting (2.17) into the above equation, note that $\mathbf{P}_M \mathbf{M}^{-1} \mathbf{B}$ is not always full column rank, implying that it might have a null space of *internal forces*. Internal forces are torques that the actuators can apply that may affect the ground-reaction and contact forces, but do not cause any motion. Let \mathbf{C} denote the matrix containing independent columns of $\mathbf{P}_M \mathbf{M}^{-1} \mathbf{B}$. Therefore, \mathbf{C} is a $n \times \text{rank}(\mathbf{P}_M \mathbf{M}^{-1} \mathbf{B})$ matrix. This matrix satisfies

$$\Delta\dot{\mathbf{q}} = \mathbf{C} \boldsymbol{\tau}'_r, \quad (2.29)$$

where $\boldsymbol{\tau}'_r$ is a reduced vector of actuator torques having the property that $\mathbf{C} \boldsymbol{\tau}'_r = \mathbf{P}_M \mathbf{M}^{-1} \mathbf{B} \boldsymbol{\tau}'$. Now, by replacing (2.29) into (2.28) we will have

$$\Delta\dot{\mathbf{q}}^T \mathbf{W}_q \Delta\dot{\mathbf{q}} = 1 = \boldsymbol{\tau}'_r^T \mathbf{C}^T \mathbf{W}_q \mathbf{C} \boldsymbol{\tau}'_r. \quad (2.30)$$

By regarding $\mathbf{W}_r = \mathbf{C}^T \mathbf{W}_q \mathbf{C}$ as a new weighting matrix, the above equation will be similar to (2.22). Given that

$$\Delta\dot{\mathbf{c}} = \mathbf{J} \Delta\dot{\mathbf{q}} = \mathbf{J} \mathbf{C} \boldsymbol{\tau}'_r, \quad (2.31)$$

we can conclude from (2.27) that (also compare (2.31) with (2.20))

$$0 \leq \Delta\dot{\mathbf{c}}^T (\mathbf{J} \mathbf{C} \mathbf{W}_r^{-1} \mathbf{C}^T \mathbf{J}^T)^{-1} \Delta\dot{\mathbf{c}} \leq 1. \quad (2.32)$$

The above equation is the equation of an ellipsoid which is characterized by the eigenvectors and eigenvalues of matrix $\mathbf{J} \mathbf{C} \mathbf{W}_r^{-1} \mathbf{C}^T \mathbf{J}^T$. This ellipsoid shows the relationship between instantaneous change of the velocity of the CoM with respect to the unit weighted norm of instantaneous changes of joint velocities. Thus, this ellipsoid represents the movement of

the CoM for a certain amount of movement at the joints. The larger this ellipsoid is, the less movement at the joints is required to move the CoM and therefore the higher the ability to recover from an unbalanced configuration. Note that, this ellipsoid includes the effect of under-actuation (due to the floating base) as well as kinematic constraints (due to the contacts) by involving \mathbf{C} instead of \mathbf{P} in the calculations (compare (2.32) with (2.11)).

Note that, the analysis presented in this section is applicable to planar robots, in which case $n = k + 3$, $\ddot{\mathbf{c}} \in \mathbb{R}^2$ and the ellipsoids become ellipses.

2.4 Application to Design and Analysis

As previously mentioned in this paper, the dynamic manipulability of the CoM is a metric that can be used to qualitatively analyse the physical ability of a mechanism to accelerate its CoM. The two proposed types of ellipsoids in section 2.3 represent the torque (energy) efficiency and maneuverability of a robot in a certain configuration. As can be seen in (2.27) and (2.32), these ellipsoids are dependent only on the physical properties of the robot (inertial parameters and dimensions), kinematic constraints and its configuration and not on the joint velocities or gravity and Coriolis forces. In other words, these ellipsoids are *configuration dependent* and not *velocity dependent*. This is a fundamental difference between the proposed analysis in this paper and those that are used in previous studies [18, 36, 58] which is due to employing impulsive dynamics for deriving the ellipsoids' equations.

The *Change-of-velocity ellipsoid—unit joint velocity* which is a metric for maneuverability is a new concept that is first introduced in this paper. Previous CoM manipulability studies only talk about relationship between CoM acceleration and joint torques by using full dynamics equations. This is comparable with our proposed *Change-of-velocity ellipsoid—unit joint torque*. If we assume a unit weighted sphere of joint torques at the actuated joints (i.e. $\boldsymbol{\tau}^T \mathbf{W}_\tau \boldsymbol{\tau} = 1$) and calculate the CoM acceleration (i.e. $\ddot{\mathbf{c}}$) via (2.12), we will end up with an ellipsoid which its radii and orientation are the same as our proposed ellipsoid in (2.27). The equation of this new (velocity dependent) ellipsoid will be

$$0 \leq (\ddot{\mathbf{c}} - \ddot{\mathbf{c}}_v)^T (\mathbf{J}_\tau \mathbf{W}_\tau^{-1} \mathbf{J}_\tau^T)^{-1} (\ddot{\mathbf{c}} - \ddot{\mathbf{c}}_v) \leq 1, \quad (2.33)$$

where

$$\ddot{\mathbf{c}}_v = -\mathbf{J} \mathbf{P}_M \mathbf{M}^{-1} (\mathbf{h} + \mathbf{g}) + \dot{\mathbf{J}} \dot{\mathbf{q}} - \mathbf{J} \mathbf{J}_{CM}^\# \dot{\mathbf{J}}_c \dot{\mathbf{q}}, \quad (2.34)$$

is the acceleration due to the gravity and Coriolis forces and also the joint velocities. Hence, physical properties of the robot and its configuration (from \mathbf{J}_τ) are the only factors that determine how much we can change the CoM acceleration of the robot with a certain amount of joint torques. Although, the total acceleration of the CoM is, of course, dependent on $\ddot{\mathbf{c}}_v$, as well. Therefore, proposed configuration based ellipsoids in this paper capture dynamic behaviours of the system which are due to its physical properties. This makes them proper metrics to measure the physical ability of a robot to accelerate its CoM and maintain its balance.

In order to use these ellipsoids for designing a new robot, one can optimize the inertial parameters and dimensions of the robot and also its configuration (i.e. all variables in \mathbf{J} , \mathbf{C} and \mathbf{J}_τ) to maximize the size of the ellipsoids in certain directions. This will maximize the

ability of the robot to accelerate its CoM in those directions. For example, maximizing the size of the ellipsoids in the horizontal directions will maximize the ability to accelerate the CoM in the horizontal and therefore increases the balance ability of the robot. For an existing robot, one can still optimize the configuration of the robot (i.e. \mathbf{q}) in order to maximize the size of the ellipsoids.

2.4.1 Joint Limits

To derive ellipsoid equations in (2.27) and (2.32), we did not consider any limits on the joint movements. Since the ellipsoids are configuration based metrics, considering joint limits makes sense only if we analyse a robot in a configuration which at least one of the joints is in (or very close to) its limit. Therefore, we define a selection matrix \mathbf{A}_j which selects the joints which are close to their limits. So,

$$\mathbf{A}_j \Delta \dot{\mathbf{q}} \leq \mathbf{0}, \quad (2.35)$$

which means that the joints that are selected by \mathbf{A}_j cannot move in one direction. Given the above new constraints, analytical solutions for the ellipsoids in (2.27) and (2.32) are not valid any more. In this case, values of $\Delta \dot{\mathbf{c}}$ will form subspaces inside those ellipsoids due to the extra constraints in (2.35). We can find those subspaces by solving (2.20) and (2.31), numerically. Note that for the first ellipsoid (2.35) will be converted to

$$\mathbf{A}_j \mathbf{P}_M \mathbf{M}^{-1} \mathbf{B} \boldsymbol{\tau}' \leq \mathbf{0}, \quad (2.36)$$

and for the second one it will be

$$\mathbf{A}_j \mathbf{C} \boldsymbol{\tau}'_r \leq \mathbf{0}. \quad (2.37)$$

The above constraints along with those in (2.22) and (2.30) determine admissible values of $\Delta \dot{\mathbf{c}}$ for the two metrics.

2.5 Experiments on Humans

To verify the application of the *change-of-velocity—unit joint impulse* ellipsoid for human studies, we perform experiments on human subjects. As already mentioned, this ellipsoid can be used to measure torque efficiency in balancing motions. So, in the experiments, we perturb the CoM of the subjects (by a cable-pulley mechanism) in different configurations and measure the contact forces/momenta with force/torque sensors (see Fig. 2.1). Then we calculate the average total torque that is done by the subjects at each configuration and compare them with the results of manipulability analysis. These steps are described in the following subsections.

2.5.1 Methods

Subjects

Eleven healthy male subjects participated in this study. Their average age was 21.7 years (SD = 2.2 years), height = 183 cm (SD = 4.6 cm) and body mass 76.8 kg (SD = 8.1 kg). The subjects were informed about the course of the study prior to their participation and were required to sign an informed consent approved by the National Medical Ethics Committee (No. 112/06/13).

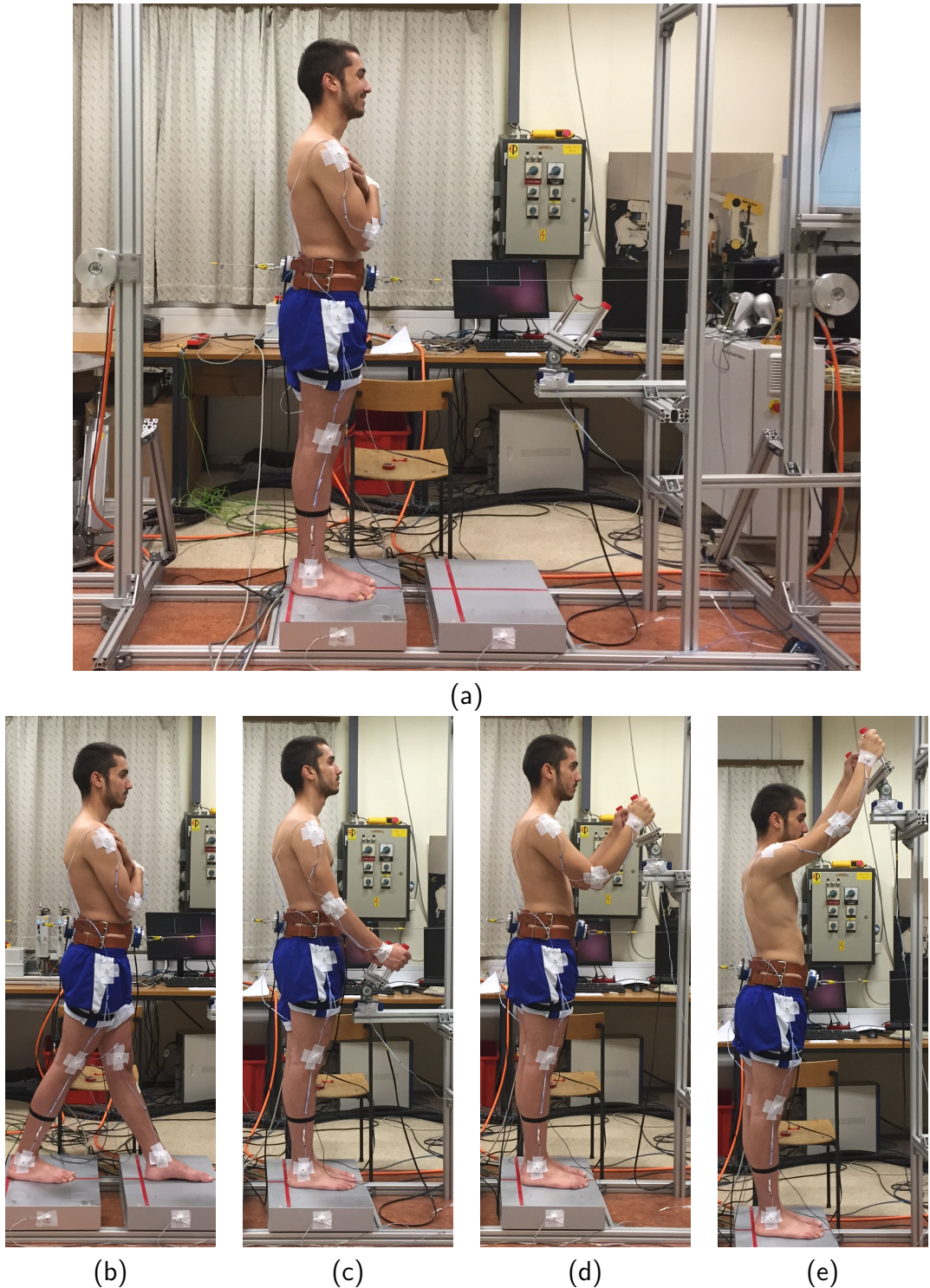


Figure 2.1: Experiments setup for five different positions: (a) stance, (b) wide stance, (c) low handle, (d) middle handle and (d) high handle. A pulley mechanism, which is connected to the subject by a belt, perturbs the subject's CoM. Contact forces are measured at the feet and hands. Motion is recorded with an optical motion capture system.

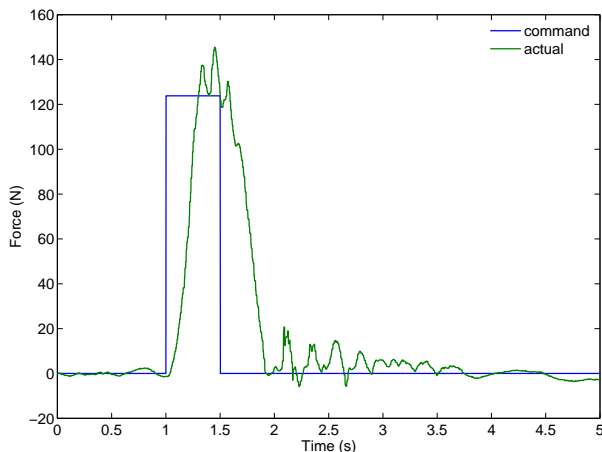


Figure 2.2: An example of the perturbation force applied to the CoM of the subjects. This is for the subject whose body mass is 76.5 kg. The intensity of the perturbation is number 6 meaning that the force is 6/8 of the maximum for this subject.

Measurement Protocol

We observed the subjects reactions to the external perturbations in five different poses. In the first pose (*stance*), subjects were standing straight with their feet together and arms crossed over the torso (Fig. 2.1.a). In the second pose (*wide stance*), subjects were standing with their arms crossed over the torso and their left foot 60 cm ahead of their right foot (ankle to ankle distance). In the third pose (*low handle*), subjects were standing as in the first pose and holding the handle which was located in front of their bodies at the hip height (Fig. 2.1.b). In the fourth pose (*middle handle*), subjects were standing as in the first pose and holding the handle which was located in front of their bodies at the shoulder height (Fig. 2.1.c). In the last pose (*high handle*), subjects were standing as in the first pose and holding the handle which was located in front of their bodies and above the head (Fig. 2.1.d).

The subjects were perturbed by a horizontal external force produced by our force-controlled pulling mechanism [60] at the approximate position of their CoM [33]. The command signal was a step with 0.5 second width (see Fig. 2.2). The actual perturbation force was controlled by a combination of a feed-forward and a PID feedback controller. We selected eight linearly increasing magnitudes of perturbation forces where the maximum was defined as 22% of the individual subject's body weight and the minimum was 1/8 of the maximum force (increasing rate of 1/8 of the maximum). Between each perturbation we induced a random pause. For each pose, we repeated the series of eight perturbations ten times (80 trials per subject per pose) and observed the human reactions. We gave the subjects 10 minutes pause between each pose. In case of the first pose, the subjects had to step before the maximum perturbation was reached. When the subject made a step, the experimenter stopped the procedure and moved to the next series of perturbations. The step was not required in other poses and the series of perturbations repeated uninterrupted.

Body movements were measured by a motion capture system (3D Investigator™ Motion Capture System, NDI, Waterloo, Ontario). The optical markers were placed on the ankle, knee, hip, shoulder, elbow and wrist. The positions of the markers are used to calculate the joint angles. We used two force plates (9281CA, Kistler Instrument AG, Winterthur, Switzerland) to

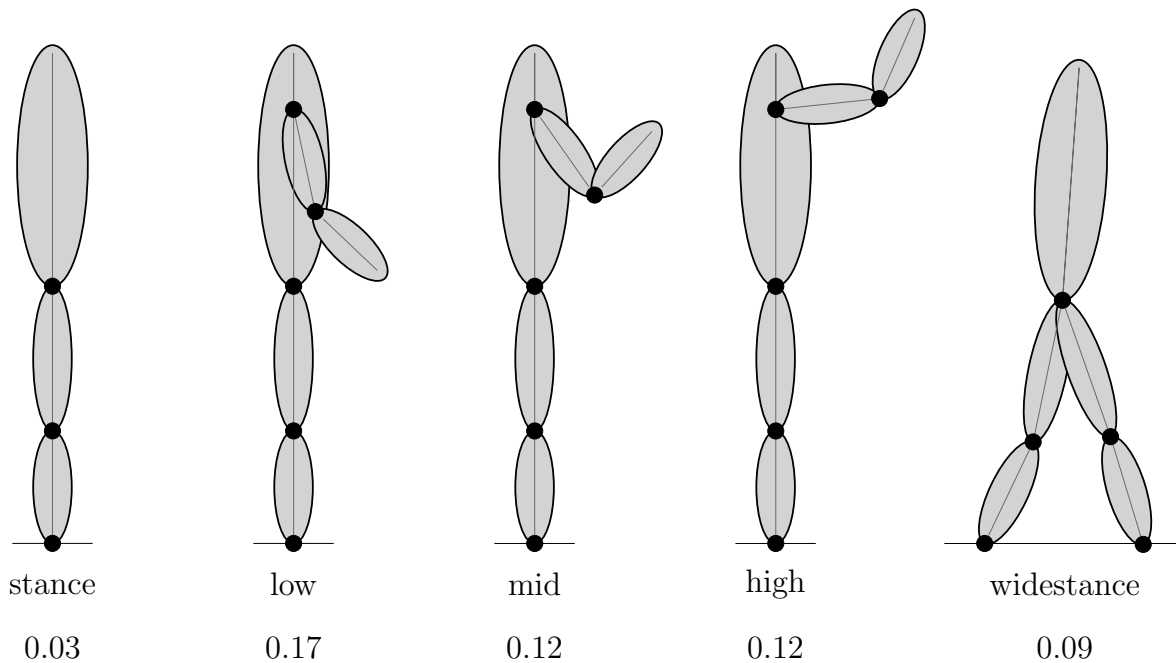


Figure 2.3: Schematic diagram of the planar humanoid robot model

measure the ground reaction forces and center of pressure position. The handle was mounted on a 3-axis force sensor (45E15A, JR3, Woodland, USA) to measure the force between the handle and the subject.

In order to estimate the starting time of the subjects' reactions, we measured muscle activation in Triceps Brachii, Soleus and Tibialis Anterior by surface electromyography (EMG). We placed surface EMG electrodes (SX230 EMG sensor, Biometrics Ltd, Newport, UK) on the selected muscles in accordance with SENIAM recommendations [38]. We also placed a monitor in front of the subject to provide visual feedback on the CoP position that allowed him to move back to the initial pose after each perturbation.

2.5.2 Model

In the experiments, in order to produce movements which are planar only, we prevented applying out-of-plane forces/moments to the subjects by providing a pair of handles for them and perturbing them in a plane. Therefore, we could use planar models for both inverse dynamics and CoM manipulability calculations. Although, using a planar model for wide stance pose is a bit unrealistic. Planar humanoid models that we used for the stance, wide stance and all three handle poses are shown in Fig. 2.3. These models consist of multiple links which are connected to each other by actuated revolute joints. Note that lower legs are connected to the ground. This is because we assume that the feet of the subjects do not move during the experiments. To model the stance pose, we lock the DoF of the arms. So, in this case, the model has 3 DoF and is unconstrained. For the wide stance, the robot has 6 DoF and is constrained due to the kinematic loop in the legs. For the handle poses, the robot has five actuated DoF and it is constrained at the hand to model the handle contact.

Since for balancing we are only interested in movements in the horizontal direction, we calculate the maximum value of $\Delta\dot{c}$ in this direction for all five positions. This represents the maximum achievable change of velocity of the CoM in the horizontal direction and is a measure for the ability to accelerate the CoM in order to correct its position in this direction. Due to the joint limits of the knees, instead of using (2.27), we use the method that is described in 2.4.1. Joint angles of the arms for the handle positions are set to the average initial joint angles of the subjects that we calculate from the marker positions. For the low handle, the shoulder angle (angle between torso and upper arm) is 12° and the elbow angle (between upper and lower arms) is 145° . Shoulder and elbow angles are 35° and 77° for the middle handle, and 96° and 118° for the high handle positions, respectively. For the wide stance position, we assume zero angles in the knees and upright torso. The weighting matrix that we use for the calculations is a diagonal matrix as

$$\mathbf{W} = \text{diag}([2.33, 3.45, 4.55, 1, 1.25]), \quad (2.38)$$

which is determined to include the differences in the joint's strengths [4, 13, 32, 57].

Calculated values for the maximum $\Delta\dot{c}$ for the five positions are mentioned in Fig. 2.3. As it can be seen in this figure, the low position has the highest value (i.e. 0.17) for the manipulability and the stance position has the lowest one (i.e. 0.03). Manipulability for the middle and high positions are the same (0.12) and lower than the low position. Also wide stance manipulability (i.e. 0.09) is only better than the stance position. Therefore, according to the manipulability analysis for our models, we expect the same ranking for the five positions in the sense of total average required torque to keep the balance. We will verify this hypothesis in the next subsection.

2.5.3 Results

As already mentioned, inverse dynamics are used to compute the torques that are applied (at the joints) by the human subjects. Joint angles are calculated by using marker positions, and joint velocities and accelerations are estimated by using simple time differentiation. Lengths and inertial parameters of the subjects are calculated via the software that is introduced in [84]. Feather stone's Spatial software package [26] is used for the dynamics calculations.

To work out the average total torque for each position and each perturbation intensity, first we calculate the joint torques from inverse dynamics for each trial (in total 4400 trials = 5 poses \times 8 intensities \times 10 reps \times 11 subjects). Then we calculate the average torque over the reps for each joint. Note that, since maximum achievable torque of the arm joints vary with arm configuration, we normalize shoulder and elbow torques for the handle positions [4, 13, 32, 57]. Then, we sum up the normalized joint torques to get 440 (i.e. 5 poses \times 8 intensities \times 11 subjects) values for the average normalized joint torques. The beginning time is the subjects' average initial reaction time which is estimated by the average EMG signal. The end time is roughly the time that the subjects have recovered from the perturbations.

The means of the normalized joint torques (per subjects) is shown in Fig. 2.4. This figure shows the total average torque (after removing outliers) for all subjects at each configuration and each intensity. The lines are fitted to the values by using least squares method. The standard error of the means are also shown in this figure. As can be seen in this figure, the low handle pose has the lowest total torque and the stance pose has the highest. According to this

Torque

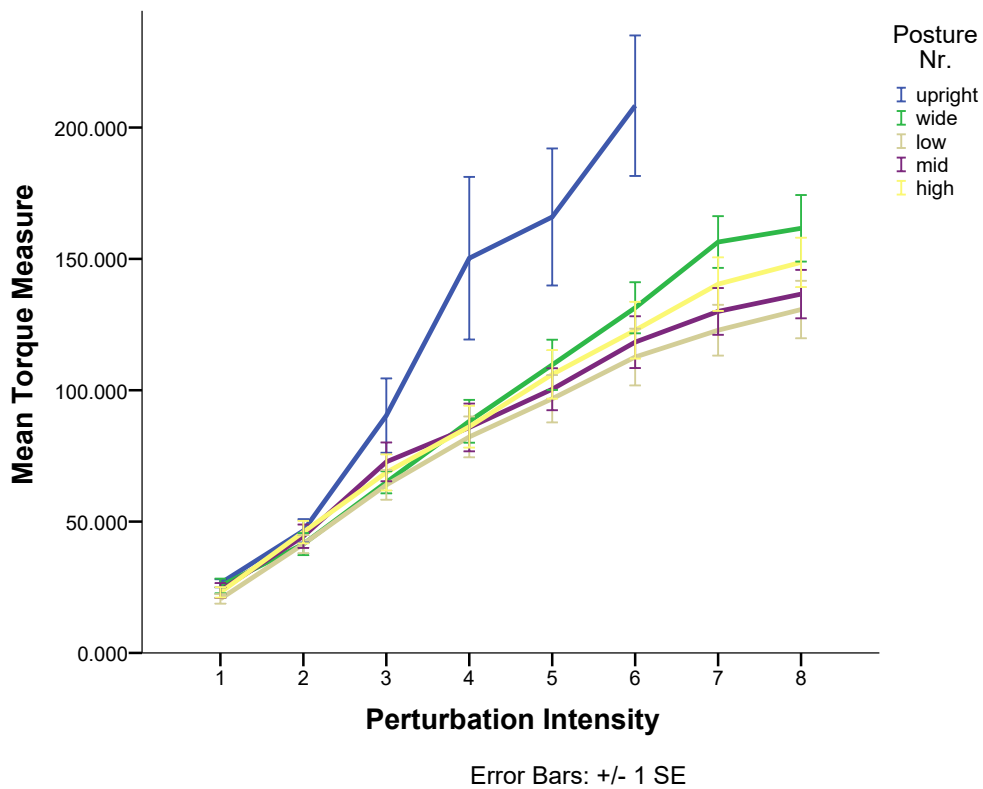


Figure 2.4: Average of the total torque for the subjects at each pose and each perturbation intensity. The stance position required the most torque in order to maintain balance. While the low handle position required the least amount of torque for the same perturbation.

graph, the ranking between the positions is 1) low, 2) middle, 3) high, 4) wide stance and 5) stance. This ranking is more visible in higher intensities and it conforms with the manipulability numbers from our analysis. The only difference is that manipulability analysis predicts that middle and high positions are the same whereas experimental results show a bit difference between two (middle is better than high). Therefore, the experimental results agree with the manipulability analysis in the previous subsection. Configurations of greater manipulability require less torque, in order to maintain balance after perturbations of equivalent magnitudes.

2.6 Conclusion

A set of metrics are introduced in this chapter to study, analyse and measure the ability to balance for humans and robots. These metrics, which are called the manipulability of the center of mass, provide two types of ellipsoids which graphically show how the CoM can be

accelerated in 3D space by a certain amount of change of motion (due to impulses) at the joint space. These ellipsoids can be used to measure torque efficiency and maneuverability of humans and robots. The proposed metrics are applicable to floating base robots with non-breakable contacts with the environment. Also, experiments on human subjects are performed to investigate the applicability of the proposed metrics for human studies. In the experiments, the standing subjects (in five different configurations) were perturbed by a controlled force acting on their CoM. Then, the selected configurations were ranked according to the average total torque that is applied by the subjects to recover their balance at each configuration. It is shown that the proposed metric for torque efficiency can successfully predict the same ranking between the configurations as the experimental results suggested. This agreement shows the applicability of the metrics for human studies as well. Therefore, manipulability of the center of mass provides greater insight into the posture controllability of humans and robots, in various configurations and contact conditions.

Chapter 3

Postural Control Precedes and Predicts Volitional Motor Control

Supportive hand contacts are essential for mastering every-day life tasks, for example, when reaching for a glass on the highest shelf humans typically have to use the other hand to support their body on the kitchen table. In such scenarios, the motion of the body and both arms have to be perfectly synchronized to successfully perform the reaching motion and to simultaneously ensure the postural stability. However, little is known about the underlying processes that govern the motion of the human body during and after the learning of these kinds of concurrent motor skills. To study the effect of supportive contacts on motor control of reaching, an innovative full-body experimental paradigm was established that extends current experimental methods to a more ecological setting. The task of the subjects was to reach with their right arm for a distant target on a screen while postural stability could only be maintained by establishing an additional supportive hand contact with their left arm. To examine adaptation, non-trivial postural perturbations of the subjects' support base were systematically introduced. A novel probabilistic trajectory model approach was employed to analyze the correlation between the motions of both arms. We found that subjects adapted to the perturbations by establishing supportive hand contacts that were dependent on the location of the reaching target. Moreover we found that the trunk motion adapted significantly faster than the motion of the arms. However, the most striking finding was that observations of the initial phase of the left arm or trunk motion (100-400 ms) were sufficient to faithfully predict the complete movement of the right arm. Overall, our results suggest that the goal-directed arm movements determine the supportive arm motions that ensure postural stability and that adaptation happens on different time scales, where the motion of heavy body parts adapts faster than light arms.

3.1 Introduction

Most of our every day motor skills involve strict control of postural stability in parallel to the execution of the primary motor task. A great deal of these tasks also require additional supportive hand contacts beside the feet that are in contact with the ground. An example task is the reaching for a glass on the highest kitchen shelf when we typically have to use the other hand to support the body by leaning on the kitchen counter. To successfully perform

such a reaching motion and to simultaneously ensure the postural stability, the motion of the body and both arms have to be perfectly synchronized and coordinated.

In general, supportive hand contacts increase the stability during balancing and complement humans' sophisticated motor abilities, e.g., in reaching for distant objects, during acrobatics or simply to navigate in the dark through leaning against a wall[17, 45, 9, 21]. Like the ability to balance, the utilization of supportive hand contacts has to be learned [63, 81]. At about two months infants are able to balance and turn their head to focus on interesting events; at six months they can balance in sitting position; at eight months infants already learn how to balance on hands and knees during crawling; at ten months they start walking with support from hanging on a table or a couch; and at about one year infants already know how to balance on two feet and walk independently across the room [2, 3]. While it is known that people develop optimal motor control strategies both for postural stability and manipulation [59, 70, 79], it is unclear how these two distinctive motor tasks relate to each other and how their relationship affect the learning of novel motor skills or when re-establishing motor abilities in novel environments. A thorough understanding of these issues is of particular interest for the field of rehabilitation, where correlations between the primary motor tasks and the underlying supportive motor actions could be exploited in progress monitoring and novel pre-tests of motor dysfunctions [25].

Many of previous studies either focus on control of postural stability [40, 51, 87, 52], study adaptation of arm reaching in confined lab environments [71, 89, 19, 22, 11], or study situations when postural stability and arm reaching are only indirectly related [30, 74, 72, 6, 46]. In our study we propose an innovative full-body experimental paradigm (Fig 3.1A) that extends current experimental methods to a more ecological setting where postural stability and manipulation skills are tightly interrelated and interdependent to each other. We hypothesize that the arm reaching motions determine the supportive hand contact strategies and that both motor tasks adapt during training. In particular, we assume that these two motor tasks are correlated which is reflected in synchronized motor executions and a significant correlation between target locations and supportive hand contacts. To effectively elaborate on these hypotheses we designed an experimental paradigm where we asked 20 healthy subjects to reach with their right arm for a target displayed on a screen while using their left arm to maintain postural stability by leaning on a table in front of them. Non-trivial postural perturbations of the subjects' support base were systematically introduced to examine adaptation and a novel probabilistic trajectory model approach was employed to analyze the correlations between the supportive arm motion and the motion of the arm to reach for the distant target.

3.2 Results

After a random interval of one to three seconds, the target was presented on the screen at one out of three possible locations (i.e., randomly at the left, the center or the right side on a horizontal bar). We motivated the subjects through a monetary reward that was proportional to the time needed to reach for the target. This reward was displayed after the target was reached. The number zero was displayed if the trial time exceeded two seconds. In our results, we focused on the y-coordinate of the contact locations as it corresponded to the direction of the translational perturbation. This is indicated by the arrow labeled by y in Fig 3.1.

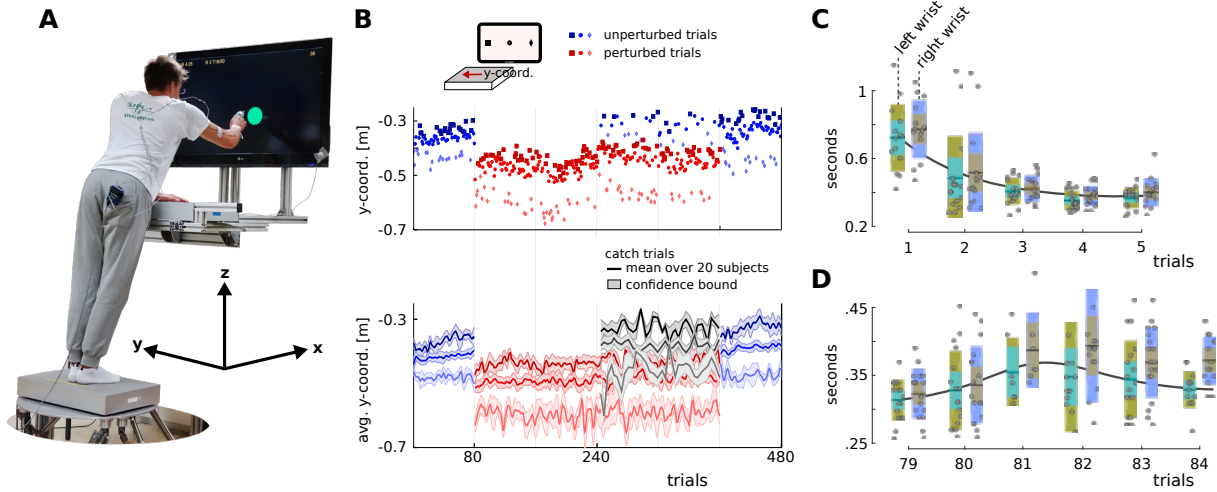


Figure 3.1: Experiment, target dependent contacts and synchronized arm motions. **A)** Experimental setting. **B)** The top row shows contact locations for a single representative subject and the bottom row shows the mean and the confidence bound over all 20 participants. The first 80 trials and the last 80 trials are unperturbed sessions. Catch trials were initiated during trials 240 to 400 and are denoted by the black lines in **B**. **C)** Illustration of the movement onsets of the wrists for the first five trials. **D)** Movement onsets for the first six trials transitioning to the perturbed session.

3.2.1 Subjects chose task dependent contact locations

Analysis of variance (ANOVA) showed a significant effect in the left hand contact location between sessions when the subjects were perturbed and unperturbed during reaching toward targets displayed on screen, $F(1, 19) = 113.632, p < 0.001, \eta_p^2 = 0.857$.

The post-hoc analysis showed that the left hand contact location was significantly different between reaching toward all three distinctly positioned targets in perturbed, $t(19) = 6.85$ to $11.58, p < 0.001$, and in unperturbed trials, $t(19) = 6.78$ – $12.21, p < 0.001$.

There were also significant differences between means of contact locations for each target between perturbed and unperturbed trials (target one, $t(19) = 10.07, p < 0.001, d = 2.01$; target two, $t(19) = 10.22, p < 0.001, d = 2.38$; target three, $t(19) = 11.51, p < 0.001, d = 3.25$), see Supplementary Fig 3.7.

Further, we analyzed individual sessions of unperturbed, perturbed and catch trials. We compared them with each other to determine whether there are any differences between contact locations and for which target positions they apply.

The first 80 trials out of 480 training trials were unperturbed. We found that there was a significant effect of target locations on the supportive contact locations in these first 80 trials, $F(1.11, 21.14) = 104.61, p < 0.001, \eta_p^2 = 0.846$, see Fig 3.1B. Post-hoc tests using the Bonferroni correction [12] revealed that there was significant difference in chosen supportive contact location between all three targets ($t(19) = 6.92$ to $11.66, p < 0.001$).

After the initial training phase, all subjects had to adapt to translational perturbations of the support base. Note that to compare the contact locations and the marker trajectories of perturbed and unperturbed trials, we corrected all sensor readings by the motion of the moving base. We refer to this correction as the *subject frame*. Later we will introduce

shoulder frames to separate adaptation in the trunk and in the arms. Again, we found that there was a significant effect of the target location on the contact location over all perturbed trials, $F(1.33, 25.27) = 116.39, p < 0.001, \eta_p^2 = 0.86$, see trials 81 to 240 in Fig 3.1B. Post-hoc tests showed a significant difference in the chosen supportive contact location among all three targets ($t(19) = 6.85$ to $11.58, p < 0.001$).

Consolidation of the postural control strategies was tested through randomly initiating unperturbed trials (catch trials). In the last phase of perturbed trials (trials 320 to 400), where adaptation can be assumed to be converged, the perturbation was deactivated for 30 random catch trials. When comparing initial training trials with catch trials post-hoc tests showed no significant difference for all three targets, target one ($t(18) = -1.99, p = 0.062, d = -0.74$), target two ($t(18) = -3.28, p = 0.004, d = -1$) and target three ($t(18) = -1.03, p = 0.315, d = -0.39$). Comparison of perturbed and catch trials showed significant differences in contact locations for all three target locations ($t(18) = -11.24$ to $-12.97, p < 0.001, d = -2.44$ to -1.93). For the washout, no significant difference was observed between contact locations for individual targets when comparing catch and final trials 401 to 480 ($t(18) = -1.59$ to $1.28, p = 0.13$ to $0.22, d = -1$ to -0.39).

In summary, we found that subjects chose distinct contact locations dependent on the target location on the screen. Catch trial tests revealed that the participants learned specialized control strategies for unperturbed and perturbed conditions. However, whether the distinct contacts result from trunk or left arm adaptations can not be answered from looking at contact locations only. That requires a more detailed analysis of the temporal profiles for which we will introduce a probabilistic trajectory model.

3.2.2 Supportive and goal-directed movements synchronize

Decreasing reaction times are an indicator for adaption of a pre-processing phase [47]. In line with this, we found that the movement onsets of the left and the right wrist synchronize within 3 – 5 trials in the unperturbed training phase (left wrist: $323 \pm 44(\text{SD})$ ms, right wrist: 335 ± 46 ms) and when the perturbations are experienced for the first time (left wrist: 333 ± 48 ms, right wrist: 342 ± 49 ms). For the first six trials, the onsets of all subjects and the computed means and standard deviations (SD) are illustrated in Fig 3.1C-D.

No significant dominance of the supportive left arm motion over the right arm reaching movements was found in the data. This is shown in an illustration of movement onsets of all subjects in Supplementary Fig 3.8.

3.2.3 Modeling joint distributions over limb trajectories

Reaction times are sensitive to signal noise, need to be verified through visual inspection and allow only for a limited view on the functional mechanisms during skill learning. As an alternative to reaction time studies, we propose to analyze adaptation on a trajectory basis. For that we developed a probabilistic trajectory model (PTM) that encodes a joint distribution over multiple limb trajectories and over multiple coordinates like x, y, z components of three-dimensional marker data. Here, we give a brief summary of PTMs and for a precise mathematical definition we refer the reader to the Methods section.

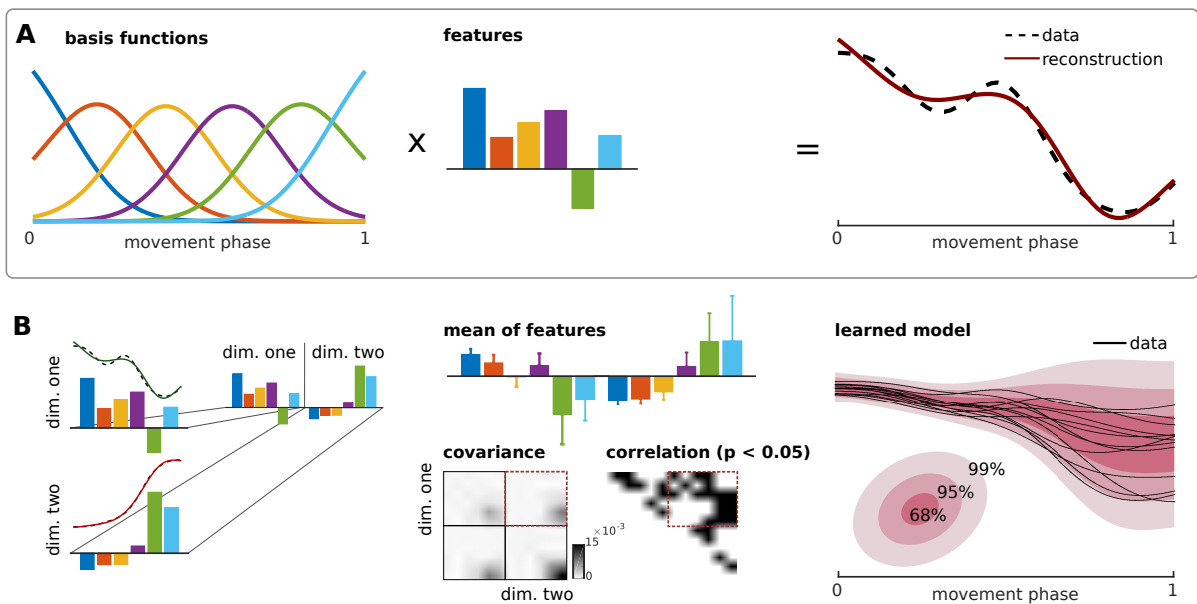


Figure 3.2: Probabilistic model of trajectories, from a feature space (left column) to trajectories (right column): A) Generative model. Equally spaced (radial) basis functions are amplitude scaled by a feature vector to approximate a one-dimensional trajectory. A movement phase substitutes time to model trajectories of different lengths. In the inverse direction, feature vectors are computed given the input trajectories using, e.g., standard linear regression techniques or iterative variational approaches like expectation-maximization. **B)** Learning the correlations between multi-dimensional input trajectories. Feature vectors computed from multiple input trajectories are concatenated and the mean and the covariance are computed from multiple trials (or subjects). The learned correlation in the center panel is the key features for computing predictions from partial observations. The distribution over trajectories is shown in the right panel.

The main feature of the model is that it captures the correlations between individual input dimensions. The model builds on a linear function approximator using radial basis functions with fixed means and variances. The amplitudes are scaled by learnable features. Now both, the basis functions and the features, form a linear generative model of a trajectory, i.e., $\tau = \Phi w$ (with the trajectory $\tau = [y_1, y_2, \dots, y_t]$, time-varying observations y_t , basis functions in Φ and feature weights w). Fig 3.2A shows the encoding of a single trajectory using classical radial basis functions. Note that the model is linear in the feature space, however it can capture non-linear dependencies in the trajectory space (through non-linear basis functions). The model's complexity is controlled through the number of basis functions. For the reaching experiments ten Gaussian distributions per dimension were found to be sufficient, see Supplementary Fig 3.9.

The feature vector w can be learned in the most simple case through standard linear regression or in more sophisticated models through one of the many existing variational inference methods [64].

A PTM encodes multiple input dimensions through a concatenated feature vector (a two-dimensional example is illustrated in Fig 3.2B). This concatenated feature vector scales the contribution of an extended basis function matrix. Thus, the only difference to standard radial

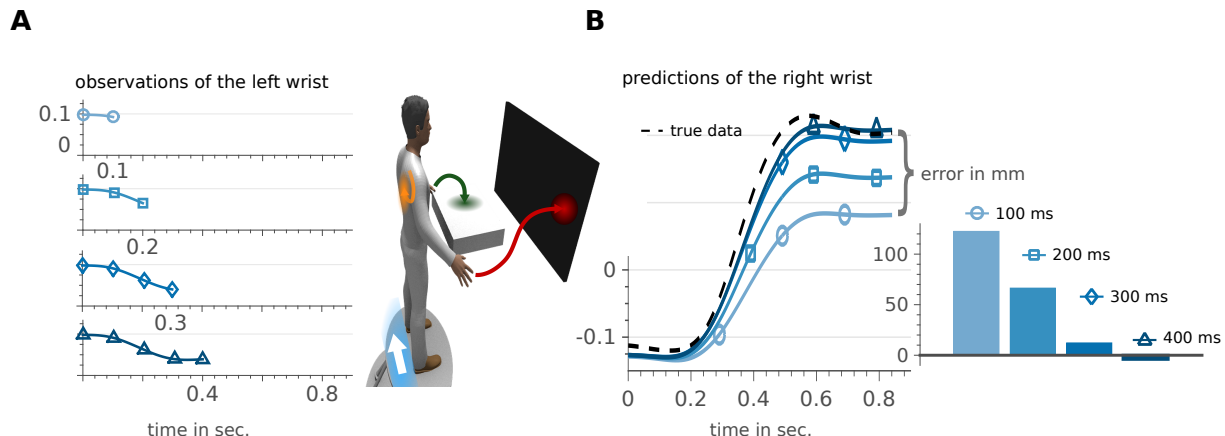


Figure 3.3: Supportive contacts predict goal-directed movements: **A)** Partial observations of the left wrist predict right wrist future states in **B**. For increasing observation horizons of the y-coordinate of the left wrist, the predicted right wrist trajectories converge to the true trajectory (illustrated as dashed line in **B**). The final Euclidean error (to the true reached target on the screen) of less than 2 cm after 300 ms is 40 times smaller than the distance between the two outer targets (that is 80 cm).

basis functions is a clever arrangement of basis functions and feature vectors to represent multiple input dimensions in one model.

To model a distribution over trajectories the mean and the covariance over multiple trials are computed from the inferred feature vectors (e.g., through linear regression). An example is shown in the center panel in Fig 3.2B. The mean and the covariance encode a distribution over trajectories in the feature space and through the relationship $\tau = \Phi w$, the distribution can be mapped (back) to the time domain. It is worth mentioning that a PTM can represent trajectories of varying lengths by substituting time by a movement phase. The last panel in Fig 3.2B shows an illustrative example of a trajectory distribution and the corresponding input trajectories using a movement phase.

To conclude, the advantage of the presented time-series model is that it can be formulated as a generative probabilistic model for which many learning algorithms and similarity measures exist. The model can encode the signal variation and can be used to compute operations like predictions, model comparisons or trial likelihoods. These operations are explored in the present study on postural control with supportive contacts.

3.2.4 Supportive contacts predict goal-directed movements

The learned and represented correlation of multiple limb trajectories can be exploited in computing predictions. This feature is used here to investigate if left wrist trajectories can predict the right wrist reaching trajectories. To separate the contributions of the trunk and the left arm, we transformed the wrist marker trajectories to a *shoulder frame*. For that the wrist positions in the subject's coordinate frame were additionally corrected by the time-varying shoulder marker positions.

For increasing observation horizons up to 400 ms, exemplary predictions of the y-coordinate of the arm trajectories are shown in Fig 3.3. For these examples the target prediction error

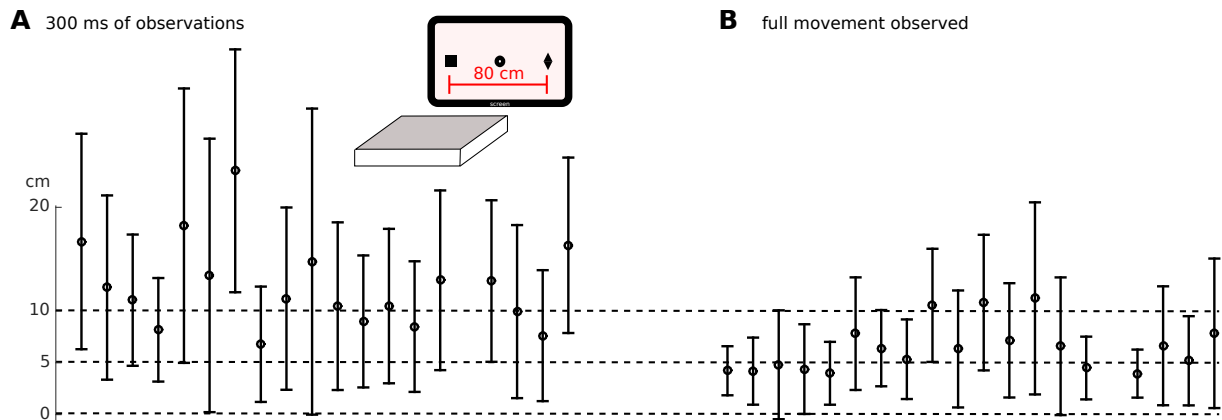


Figure 3.4: Target prediction error over all subjects: **A)** Averaged prediction error for 19 subjects when observing 300 ms of the left wrist marker trajectories in perturbed trials. **B)** The prediction error when observing the whole left wrist motion. Illustrated are the mean and the standard deviation over 18 test trials (six per target). One subject of 20 was excluded as less than six trials per target were recorded. Note that the maximum error or the distance between the two outer targets in the screen is 80 cm.

was below 5 cm when observing only the first 300 ms of the left wrist motion. Note that the distance between the two exterior targets on the screen was 80 cm which defines the maximum error. Averaged over all subjects, the prediction error was 12.3 ± 9.8 cm for an observation horizon of 300 ms. When observing the complete trial the error was 6.4 ± 5.5 cm. Per subject errors are shown in Fig 3.4. Note that to obtain these results we used 18 trials for training (trials 170 – 320) and 18 trials for testing (trials 321 – 400).

In summary, the PTM was used to train models of trajectory distributions that could predict the goal-directed reaching motions from observing solely the supportive left wrist movements. Accurate predictions at an early execution phase (i.e., the first 300 ms), where the effect of visual feedback is negligible, indicate that supportive contacts are at least partially pre-processed.

3.2.5 Trunk adaptation precedes arm adaptation

To investigate adaptation of the supportive contacts we fitted Gaussian distributions to the contact locations recorded in the three phases of learning — the unperturbed training phase, the phase of perturbed trials and the final washout phase. Histograms over the contact locations in the shoulder frame are shown in Fig 3.5A, where *UP1* denotes the initial training phase, *P* the perturbed trials and *UP6* the sixth session that was the washout phase. During the perturbed trials of the experiment, we found a shift of contacts to the right, or in other words, the left hand is moving closer to the center of the table in Fig 3.1A (Note that the particular values in meters differ in Fig 3.1A and in Fig 3.5A. In the later the contacts are plotted in the shoulder frame).

To compare the similarities between the fitted Gaussian distributions for the three phases of learning, we used a Kullback-Leibler divergence (KL) distance measure. In line with the observation of the shift of contacts, we found strong similarities between the unperturbed

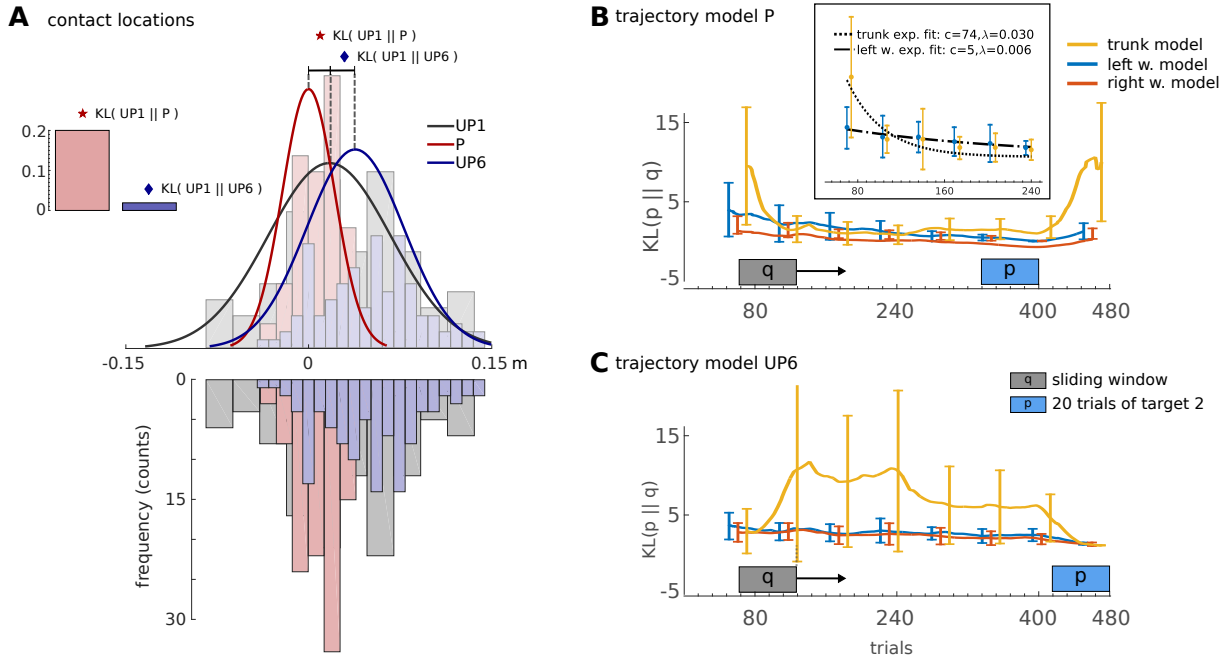


Figure 3.5: Trunk adaptation precedes arm adaptation: **A)** The adaptation process of the contact location is illustrated by computing the KL-divergence between the first unperturbed session (UP1), the perturbed trials (P), and the last unperturbed session (UP6). The underlying data is shown as histogram with the Gaussian model fits as overlay. **B-C)** For a detailed temporal analysis, the KL-divergence between a set of training trials (a sliding window of 20 trajectories) and a set of test trials (**B**: last 20 trials in P, **C**: last 20 trials in UP6) is investigated. An exponential model fit is presented in the inset in **B**.

phases, i.e., $KL(UP1||UP6) = 0.019$. In contrast for the transition to the perturbed trials we computed a distance of $KL(UP1||P) = 0.20$. For the transition to the washout phase, we found $KL(P||UP6) = 0.126$.

A more detailed investigation was conducted by analyzing trajectory similarities using the PTM. As reference model, trajectories of the last 20 trials in P or UP6 were used. We compared the reference model to a trajectory model trained from 20 trials in a moving window. The moving window traverses from trial 10 to trial 460 which is denoted by the shaded boxes in Fig 3.5B and C. Individual models were trained for the left wrist, the right wrist and the trunk. We found that the trunk model converged about five times faster than the left wrist model. For that we used one-term exponential models of the form $y = c \exp(\lambda x)$, where for the trunk $\lambda_t = 0.03$ and for the left wrist $\lambda_l = 0.006$. This result is highlighted in the inlay in Fig 3.5B.

We found that the trunk adapts faster than the supportive contact motion. This finding can be explained by the importance of correct trunk motions to prevent falling as observed in related work [14, 74]. When comparing the prediction accuracy however, we made an interesting observation. During early phases of the motor execution the left wrist results in more accurate predictions. However, when observing the complete motion, the trunk was more informative for predicting the right arm movements, see Supplementary Fig 3.10. This result suggests that the supportive motion has a stronger effect on the task performance during early

phases compared to the massive trunk.

3.3 Discussion

It is known that supportive contacts aid postural control in humans [9]. Contacts increase the subjects' belief about their poses in board balancing tasks [72], in tasks without visual cues [46], and have an effect on learning balancing strategies during task adaptation [6]. While these studies demonstrated the importance of contacts for human motor control, the contacts were *static* and pre-defined based on the experimental setting. In this study, we investigated the effect of the *active choice* of supportive contacts on motor control. Under natural conditions subjects were able to choose supportive contact locations to aid target reaching. Utilizing a developed probabilistic trajectory model (PTM), we found that the supportive motions leading to contacts could predict goal-directed reaching movements and learning proceeds on multiple time scales. These findings have important implications on medical care in diseases related to central nervous system disorders (such as dementia, Alzheimer's, Parkinson's disease or stroke), computational neuroscience and robotics.

3.3.1 A pre-test for central nervous system disorders affecting postural control

Many central nervous system disorders affect not only cognitive abilities related to memory consolidation but also postural control. For example, an underdevelopment of postural control is a well known symptom in autism[69, 56]. Early detection of these diseases is of utter importance for medical care. However, most pre-tests focus on cognitive functions that are influenced by many factors such as stress, sleep deprivation and age. Classical tests targeting motor coordination abilities are unnatural like for example the grooved pegboard test[48], where the goal is to fit pegs of various shapes into punched holes. The presented experimental setting has the potential to become an alternative pre-test that investigates postural control and motor learning under natural conditions. Deficits in motor control can be quantified in terms of the model prediction performance as shown in Fig 3.3. In the tested subjects, the average prediction error of the goal-directed target reaching motion was 6.4 ± 5.5 (SD) cm out of a total range of 80 cm. Note that for these predictions the model input was solely the x,y,z coordinate of the supportive motion, see Fig 3.4B. While the predictions were accurate for the tested healthy subjects, we speculate that participants with motor dysfunctions would show inferior prediction performance scores.

However, a limitation of the presented experimental setting is its simplicity. In our experiments the participants reached for a static target at one out of three possible locations on a horizontal line. Synchronization of movement onsets within 3 – 5 trials (see Fig 3.1C-D) indicates that the task might be too simple to show significant effects in subjects with central nervous system disorders. More complex tasks could consider for example moving targets at arbitrary locations on the screen.

3.3.2 Evidence for learning on multiple time scales

For many tasks motor memory consolidation proceeds on different time scales[88, 73, 22]. In particular, postural control is adapted on a faster rate in contrast to goal-directed movements. For example, Huys et al. showed that postural sway precedes eye and head movements (3 : 2 or also 3 : 1) in subjects learning to juggle[41]. In line with this finding, we found that trunk adaptation to maintain balance precedes the learning of optimal (here task correlated) supportive contact motions. Concretely, the learned trunk model converged about 5 times faster than the left wrist model, see Fig 3.5B. This result is another indicator for a hierarchical organization of motor control with the difference that we analyzed adaptation on a trajectory level in contrast to single time step models [51, 88, 22]. The developed PTM may extend future computational models for optimal feedback control by combining sequential predictions of feed forward commands and the integration of perceptual feedback.

A potential deficit of such an optimal feedback controller is that we analyzed adaptation on a kinematic level, where limb inertia has a delayed effect on the recorded marker trajectories. For example, while expressive motion vectors can be observed for the light weight arms, the massive trunk may have moved just for few millimeters which could result in inaccurate predictions. This hypothesis is confirmed by our results, where at early movement phases (up to 300 ms) the left wrist leads to more accurate predictions than the trunk, see Supplementary Fig 3.10. For observations of the complete trial however, the trunk motion is more informative. To avert the effect of limb inertia the PTM could be trained from Electromyography (EMG) patterns. Such models could be used to predict motor commands on a muscle level and could help to better understand the underlying motor control mechanisms.

3.3.3 A robot controller that actively seeks for contacts

In this research we studied whole-body coordination mechanisms of arm reaching and postural control with additional hand contact. We investigated how humans perform reaching movements with the right arm in postural challenged conditions. Postural balance was maintained by establishing a supportive hand contact with the other arm. In effect, both arms had to perform reaching movements where one arm reaches for a distant target and the other arm reaches for a supportive hand contact. We found that humans preferred distinct contact locations for each of the three targets that were displayed. Such a context dependent controller could advance current abilities of humanoid robots as it was envisioned in the European project CoDyCo[1]. In particular, our results suggest that different supportive contact strategies should be initiated based on future intentions. This has not been done so far as research on anticipatory controller focused largely on balancing[77, 66, 78] or on compensating for external forces[5, 42, 67, 80].

In our experiments the modulating factors (the context) were the distance to the target, its location on the screen and the postural perturbation. The distance was chosen such that subjects *always* made a contact to avoid falling when reaching. We only investigated the effect of the contact location and used pre-defined translateral support base perturbations. The perturbations had no effect on the results. In unperturbed and perturbed conditions the subjects chose target dependent contact locations, see Fig 3.1B. Future research may explore the effect of distance to complement a robot controller that autonomously decides in which

situations to make supportive contacts.

3.4 Methods

3.4.1 Participants

Twenty right-handed male subjects (age: 20.8 ± 1.8 (SD)) participated in the reaching experiments. None reported any neurological or musculoskeletal disorders (self-reported). Prior to their participation, the subjects were informed about the course of the study and were required to sign an informed consent approved by the National Medical Ethics Committee Slovenia (NO. 112/06/13).

3.4.2 Apparatus

Participants stood on a force plate (9281CA, Kistler Instrumente AG, Winterthur, Switzerland) mounted on top of a Stewart platform [75]. The force plate was used to measure the six components of the ground reaction forces and torques to determine the center-of-pressure (CoP). The CoP was only used to pre-compute tentative movement onsets (based on two percent peak velocity and CoP criteria). These pre-computed movement onsets of the left and the right wrist were manually corrected through visual inspection (480×20 trials).

A second force plate of the same type was mounted anteromedial to the subject's hip position. This force plate was used like a table providing additional support during reaching. The contact locations shown in Fig 3.1 were defined as the left wrist position at the peak supportive contact force. In front to the contact force plate we mounted a screen. Both, the force plate and the screen were adjusted in height based on the subject's trunk height (56.5 ± 2.4 cm).

The Stewart platform was used to apply translational perturbations in the mediolateral direction. Specifically, the displacement of the platform was proportional to the sum of the anteroposterior components of the left and right hand displacements. The maximal displacement of the Stewart platform was 20 cm and corresponded to the situation when the subject's left hand was at the far edge of the table and the finger on the right hand touched the screen, see Supplementary Fig 3.6.

A motion capture system (NDI 3D Investigator) was used to track the participants wrists and trunk movements. Three motion tracking markers were attached to each wrist to compensate for occlusions during the reaching motions. At least one marker needed to be visible and for more than one visible marker the position was computed through averaging. Two markers were attached to the back at the scapulae to transform wrist trajectories to shoulder frames and to estimate the trunk motions (i.e., the center location of the two shoulder markers). Additional markers were placed at the screen, at a wearable thimble to estimate the right index fingertip position and at the force plate mounted on top of the Stewart platform.

3.4.3 Coordinate frames

If not stated different, the results are defined in the subject's coordinate frame. To compensate for the translational perturbations of the Stewart platform a marker was attached to the support

force plate. The subjects coordinate frame was defined as the force plate marker position minus the initial left wrist location (to correct for small deviations of the subject's feet placement throughout the experiment).

Wrist trajectories (see Fig 3.3) were computed in the shoulder frames to isolate trunk and arm adaptations. In particular, the wrist positions in the subject's coordinate frame were additionally corrected by the time-varying shoulder marker positions.

3.4.4 Procedure

Participants had to perform 480 trials of reaching in blocks of 80 trials. After each block the subjects had a five minutes break. Only the first and the last 80 trials were unperturbed (see Fig 3.1b). To investigate negative after effects, the perturbation was deactivated for 30 randomly selected reachings during trials 240 to 400. The participants were not informed about these catch trials.

Prior to each trial, subjects were required to stand upright moving as little as possible. A bar on the screen indicated anteroposterior fluctuations of the CoP in real time with respect to the initial CoP value. This initial CoP was measured at the beginning of the experiment. If the mean of the deviations averaged over 500 ms was less than 1 cm the start of the trial was initiated. After one second the target was presented at one out of three locations (target onset). After a random period (1 – 3 sec) the target's color switched and the subjects were allowed to move. Movements prior to that visual cue terminated the trial. The target was reached if the distance between the fingertip and the target on the screen was less than 1 cm.

Participants received a monetary reward after each trial based on the time needed for reaching, i.e., $\text{EUR} = 0.1 - 0.05t$ where t denotes the reaching time in seconds. The reaching time was defined as the difference between the target onset and the time until the target was reached. On average the subjects received five cents per trial which corresponds to a reaching duration of one second, see Supplementary Fig 3.11. If the target was missed, or if the target was not reached within two seconds, no reward was given.

3.4.5 Data processing

All measurements of the force plates and the motion capture system were recorded at a rate of 100 Hz. Redundant marker settings on the wrists and on the thimble were used to compensate for occlusions. For that three markers were used for both wrists and the thimble. If all markers were occluded the trial was excluded from the analysis. For two or three correctly observed markers we computed the average for each coordinate (x,y,z). All marker trajectories were low-pass filtered at 5 Hz using 2nd-order Butterworth filter.

3.4.6 Statistical tests

Statistical analyses were performed using SPSS 21 (SPSS Inc., Chicago, USA). For each subject, an average of left hand contact location in mediolateral direction was calculated for every combination of balance perturbation (unperturbed, perturbed and unperturbed catch trials) and target locations. The average values of the individual subjects were then used for statistical analysis. Effect of perturbation was investigated using one-way repeated measures

ANOVA. Differences between perturbed and unperturbed sessions for each combination of independent variables were tested with post hoc t-tests with Bonferroni correction. The level of statistical significance was set to 0.05.

3.4.7 Computing predictions through conditioning

Conditional probabilities and predictions are related concepts in statistical modeling. A prediction problem can be modeled as computing the conditional probability denoted by

$$p(B | A) = p(A, B) / p(A) , \quad (3.1)$$

where A and B represent two random variables (RVs). In our experiment, the variable A could encode the probability of a certain contact location on the table and the target location is represented by the RV B . The joint distribution $p(A, B)$ is the learned model and $p(A)$ is a prior over all possible contact locations. Given a particular contact location $p(A = a)$, we can compute the most likely target the human tries to reach. Throughout the paper, we will use the shorthand $p(a)$ to denote $p(A = a)$, which is the probability that the RV A takes the value a to keep the notation uncluttered.

A particularly interesting class of distributions are Gaussian distributions

$$N(\mathbf{x} | \boldsymbol{\mu}, \boldsymbol{\Sigma}) := \frac{1}{(2\pi)^{n/2} \sqrt{\det \boldsymbol{\Sigma}}} \exp \left(-\frac{1}{2} (\mathbf{x} - \boldsymbol{\mu})^T \boldsymbol{\Sigma}^{-1} (\mathbf{x} - \boldsymbol{\mu}) \right) , \quad (3.2)$$

with the n -dimensional RV $\mathbf{x} \in \mathbb{R}^n$, the mean $\boldsymbol{\mu}$ and the variance $\boldsymbol{\Sigma}$. In Gaussian distributions, conditional distributions can be computed in closed form. To see this, we define a multivariate normal distribution by concatenating two RVs. The two RVs denote the contact locations and the targets, i.e., $\mathbf{x} = \begin{pmatrix} a \\ b \end{pmatrix}$, $\boldsymbol{\mu} = \begin{pmatrix} \mu_a \\ \mu_b \end{pmatrix}$ and $\boldsymbol{\Sigma} = \begin{pmatrix} \Sigma_{aa} & \Sigma_{ab} \\ \Sigma_{ba} & \Sigma_{bb} \end{pmatrix}$. Using these definitions in (3.2) and after rearranging the terms, the parameters $\mu_{b|a}$ and $\Sigma_{b|a}$ of the conditional distribution can be computed as

$$\begin{aligned} p(b | a) &= N(b | \mu_{b|a}, \Sigma_{b|a}) , \\ \text{with } \mu_{b|a} &= \mu_b + \Sigma_{ba} \Sigma_{bb}^{-1} (a - \mu_a) , \\ \text{and } \Sigma_{b|a} &= \Sigma_{bb} - \Sigma_{ba} \Sigma_{bb}^{-1} \Sigma_{ab} . \end{aligned} \quad (3.3)$$

Given multiple measurements of a and b we can compute the statistics $\boldsymbol{\mu}$ and $\boldsymbol{\Sigma}$. For some during training unseen contact location a^* we can now predict the most likely target location (parametrized through $\mu_{b|a^*}$ and $\Sigma_{b|a^*}$). In the following we will extend this powerful feature of computing predictions to time-series data or trajectories.

3.4.8 Phase modulated probabilistic models of trajectories

The same conditioning operation can be used for computing predictions in trajectories if the RVs encode feature vectors in function approximation, see Fig 3.2 for a sketch. Let $\mathbf{y}_t = \begin{pmatrix} a_t \\ b_t \end{pmatrix}$ denote a concatenated state at time t representing the contact location and the target. Only for the sake of clarity we will again assume that the contact location and the target are scalars. As we will see later the results generalize to multi-dimensional states. In addition, we

will assume for simplicity that each dimension in \mathbf{y}_t is approximated through a J -dimensional feature vector $\mathbf{w} \in \mathbb{R}^{J \times 1}$ and basis function vectors $\phi_t \in \mathbb{R}^{1 \times J}$, e.g. $a_t = \phi_t \mathbf{w}_a$ with $\phi_t = [\phi_{t,1}, \dots, \phi_{t,J}]^T$. A large variety of possible basis functions can be used for time series approximation. A popular choice for rhythmic movements are Von-Mises basis functions, whereas Gaussian basis functions are widely used for point to point movements [65, 43]

$$\phi_{t,i} = \frac{1}{\mathcal{Z}} \exp \left(-\frac{1}{2h} (z(t) - c_i)^2 \right) ,$$

where $\mathcal{Z} = \sum_{l=1}^J \exp(-1/2h(z(t) - c_l)^2)$ denotes a normalization term. The function $z(t)$ implements a mapping from discrete time steps to a movement phase, i.e., $z : t \in [1, T] \mapsto [0, 1]$. In this notation state sequences of different length can be modeled and are aligned through the movement phase. Note that in our reaching experiments $z(t) = 0$ denotes the movement onset and $z(t) = 1$ the event when the target was reached. The scalar $c_i \in [0, 1]$ denotes the center of the i -th basis function and h is the bandwidth parameter.

In general, D -dimensional states can be approximated in $\mathbf{y}_t = \Phi_t \mathbf{w}$ using block diagonal matrices $\Phi_t \in \mathbb{R}^{D \times JD}$ and concatenated feature vectors $\mathbf{w} = [w_1^T, \dots, w_D^T]^T \in \mathbb{R}^{JD \times 1}$. For example, when modeling contacts and targets, $\mathbf{w} = [w_a^T, w_b^T]^T$ and a block diagonal matrix of the form $\Phi_t = \begin{pmatrix} \phi_t & 0 \\ 0 & \phi_t \end{pmatrix}$ is used.

Sequences of T states, denoted by $\tau = \mathbf{y}_{1:T}$, can be compactly represented by

$$\tau = \Phi_{1:T} \mathbf{w} \quad \text{with} \quad \Phi_{1:T} = [\Phi_1^T, \dots, \Phi_T^T]^T \in \mathbb{R}^{TD \times JD} , \quad (3.4)$$

where $\Phi_{1:T}$ denotes an extended basis function matrix. Using the function approximation in (3.4) we can define the generative probabilistic model for trajectories

$$p(\tau | \mathbf{w}) = \prod_{t=1}^T \mathcal{N}(\mathbf{y}_t | \Phi_t \mathbf{w}, \Sigma_y) = \mathcal{N}(\mathbf{y}_{1:T} | \Phi_{1:T} \mathbf{w}, \Sigma_y) ,$$

where Σ_y models zero mean independent and identically distributed (i.i.d.) Gaussian noise in $\mathbf{y}_t = \Phi_t \mathbf{w} + \epsilon_y$ with $\epsilon_y \sim \mathcal{N}(\epsilon_y | \mathbf{0}, \Sigma_y)$. In order to represent a distribution over trajectories $p(\tau)$, we can apply the product rule shown in (3.1) and compute the marginal. For Gaussian distributions, in particular for $p(\mathbf{w}) = \mathcal{N}(\mathbf{w} | \mu_w, \Sigma_w)$, the marginal can be computed in closed form

$$\begin{aligned} p(\tau) &= \int p(\tau | \mathbf{w}) p(\mathbf{w}) d\mathbf{w} \\ &= \int \mathcal{N}(\mathbf{y}_{1:T} | \Phi_{1:T} \mathbf{w}, \Sigma_y) \mathcal{N}(\mathbf{w} | \mu_w, \Sigma_w) d\mathbf{w} \\ &= \mathcal{N}(\mathbf{y}_{1:T} | \Phi_{1:T} \mathbf{w}, \Phi_{1:T} \Sigma_w \Phi_{1:T}^T + \Sigma_y) . \end{aligned} \quad (3.5)$$

The mean μ_w and the covariance matrix Σ_w can be learned from data by maximum likelihood using the Expectation Maximization (EM) algorithm [20]. A simpler solution that works well in practice is to compute first the most likely estimate of $\mathbf{w}^{[i]}$ for each trajectory $\tau^{[i]}$ independently, where the index i denotes the i -th demonstration. In particular, given the

trajectory $\tau^{[i]}$, the corresponding weight vector $w^{[i]}$ can be estimated by a straight forward least squares estimate

$$w^{[i]} = (\Phi_{1:T}^T \Phi_{1:T} + \lambda I)^{-1} \Phi_{1:T}^T \tau^{[i]} . \quad (3.6)$$

Subsequently, the mean and the covariance of $p(w)$ can be estimated by the sample mean and sample covariance of the $w^{[i]}$ vectors.

3.4.9 Computing predictions in trajectories

Let us assume that we have observed a sequence of states y_{t_1} to y_{t_M} at $m = 1, 2, \dots, M$ different time points, which do not need to be sampled at uniform intervals. In addition, not all of the dimensions in the vector y_{t_m} might be observed (e.g. due to occlusions, where irrelevant dimensions are assumed to be set to some real number). We introduce the homogeneous covariance matrix Σ_o to control the importance of the observations, where small diagonal variances denote important dimensions and large scalars irrelevant dimensions. For example, we would use $\Sigma_o = \begin{pmatrix} 1e-5 & 0 \\ 0 & 1e5 \end{pmatrix}$ if only the first out of two dimensions is observed (as in the example with contact locations and targets). Let us further denote Φ_o as the concatenation of the basis function matrices for these time points and o as concatenation of the y_{t_m} vectors. Given these observations, we can obtain a conditioned distribution $p(w|o)$ over the weight vectors

$$\begin{aligned} p(w_o | o) &\propto \mathcal{N}(o | \Phi_o w_o, \Sigma_o) p(w) \\ &:= \mathcal{N}(w_o | \mu_{w|o}, \Sigma_{w|o}) , \\ \text{with } \mu_{w|o} &= \mu_w + \Sigma_w \Phi_o^T (\Sigma_o + \Phi_o \Sigma_w \Phi_o^T)^{-1} (o - \Phi_o \mu_w) , \\ \text{and } \Sigma_{w|o} &= \Sigma_w - \Sigma_w \Phi_o^T (\Sigma_o + \Phi_o \Sigma_w \Phi_o^T)^{-1} \Phi_o \Sigma_w , \end{aligned}$$

which recovers the conditioning result in (3.3) in the feature space.

To predict the state sequence $\tilde{y}_{1:T}$, the conditional distribution is projected back into the trajectory space using (3.5). The result is a distribution over trajectories

$$p(\tilde{\tau}) = \mathcal{N}(\tilde{y}_{1:T} | \Phi_{1:T} \mu_{w|o}, \Phi_{1:T} \Sigma_{w|o} \Phi_{1:T}^T + \Sigma_y) , \quad (3.7)$$

where for $t_M < T$ in the observations $o = [y_{t_1}, y_{t_2}, \dots, y_{t_M}]$ future states can be predicted.

3.4.10 Computing model comparisons in trajectories

Using the proposed probabilistic trajectory model (PTM), two trajectory models can be compared through computing the Kullback-Leibler (KL) divergence. For Gaussian distributions as in (3.5) the KL divergence can be computed in closed form

$$\text{KL}(\mathcal{N}_1 || \mathcal{N}_2) = \frac{1}{2} \log \frac{|\Sigma_2|}{|\Sigma_1|} - n + \text{tr}(\Sigma_2^{-1} \Sigma_1) + (\mu_2 - \mu_1)^T \Sigma_2^{-1} (\mu_2 - \mu_1) ,$$

where \mathcal{N}_1 denotes a Gaussian with the n -dimensional mean μ_1 and the covariance Σ_1 . The symbol tr denotes the matrix trace.

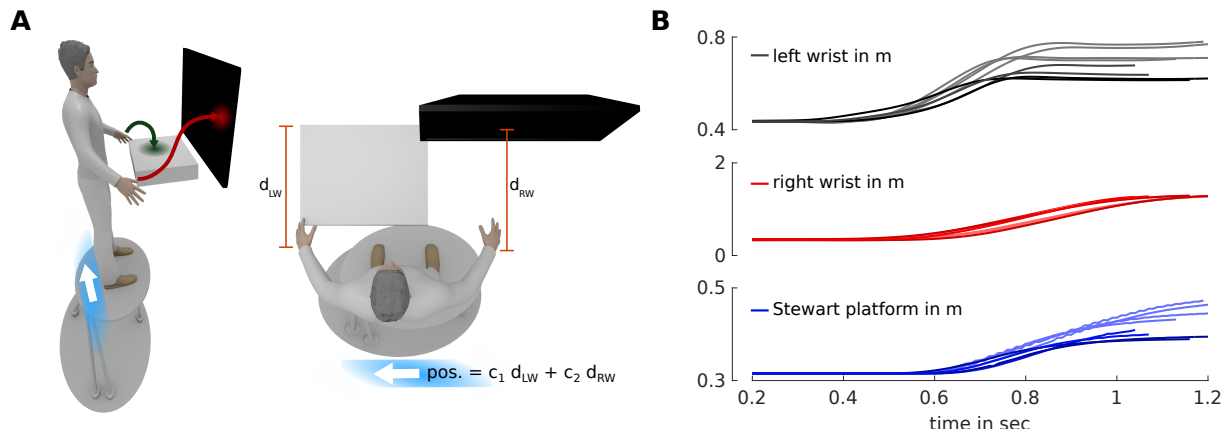


Figure 3.6: **Supplementary figure, Translateral perturbations:** **A)** The Stewart platform was used to apply translational perturbations in the mediolateral direction. Specifically, the displacement of the platform was proportional to the sum of the anteroposterior components of the left and right hand displacements. This is denoted by d_{LW} and d_{RW} with the constants c_1 and c_2 . The maximal displacement of the Stewart platform was 20 cm and corresponded to the situation when the subject's left hand was at the far edge of the table and the finger on the right hand touched the screen. **B)** Sample trajectories of the left wrist, the right wrist and the displacement of the platform.

3.4.11 Computing task likelihoods in trajectories

Another important probabilistic operation is the computation of the task likelihood. This operation can be used to test which candidate model out of several best explains the data. Let $\mathcal{N}_p(\cdot | \mu, \Sigma)$ denote the model under test. Given a single trajectory sample τ^* and its feature space representation w^* we can compute

$$\begin{aligned} L(w^* | \mathcal{N}_p) &= \log \mathcal{N}_p(w^* | \mu, \Sigma) \\ &= -\frac{1}{2}(\mu - w^*)^T \Sigma^{-1} (\mu - w^*) + \text{a constant ,} \end{aligned}$$

which quantifies how likely $\tau^* = \Phi_{1:T} w^*$ was generated by model $\mathcal{N}_p(\cdot | \mu, \Sigma)$.

3.5 Supporting Information

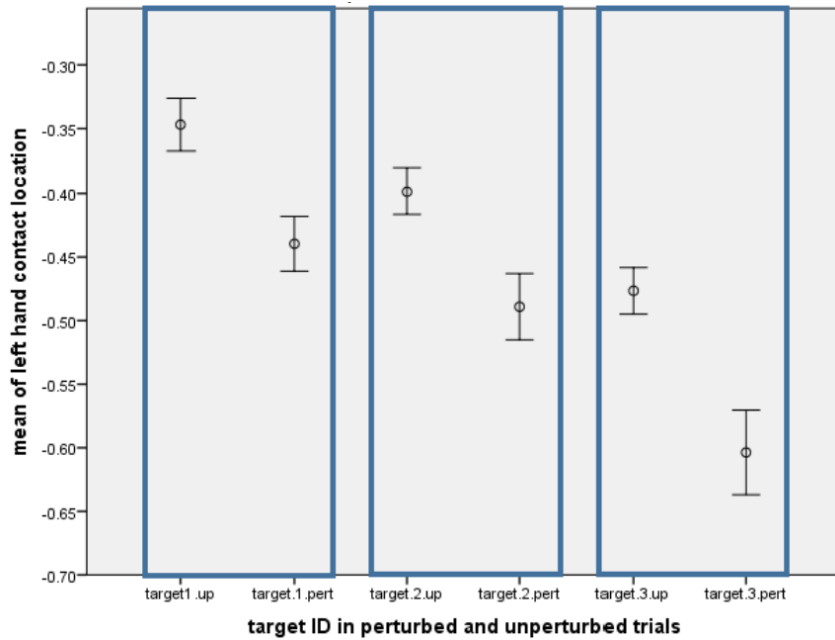


Figure 3.7: **Supplementary figure, Means of the contact locations:** From left to right the means are shown for the three target locations, where we contrast in each panel the unperturbed and the perturbed session.

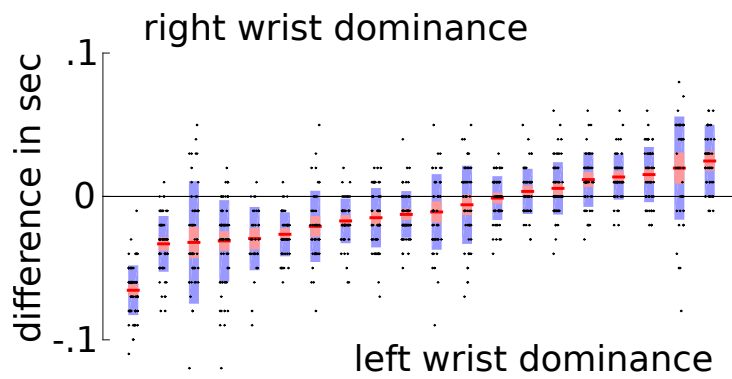


Figure 3.8: **Supplementary figure, Dominance of the left wrist in 12 out of 20 subjects:** We show the difference of the movement onsets (left wrist minus right wrist). The underlying data are representative trials of the 2nd perturbed session (170 to 240), where learning converged. The movement onsets were manually corrected through visual inspection.

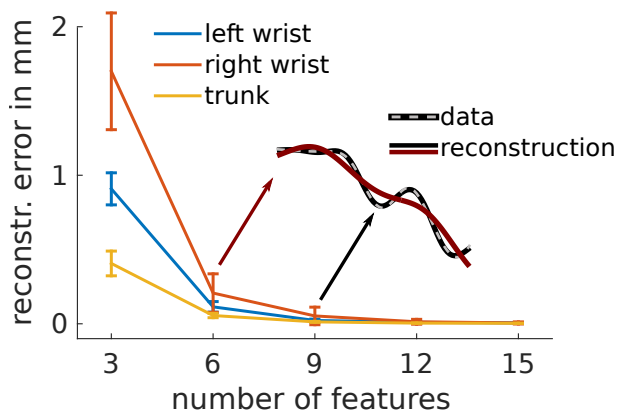


Figure 3.9: Supplementary figure. Model complexity (number of basis functions) determines the reconstruction error: With an increasing number of basis functions the reconstruction error (shown in millimeter) decreases. The reconstruction error is defined as the Euclidean distance of the generated trajectory to its observed counterpart. For the three limbs, left wrist, right wrist and trunk, the error converges to zero with more than nine basis functions. Ten basis functions are used in the experiments in the manuscript.

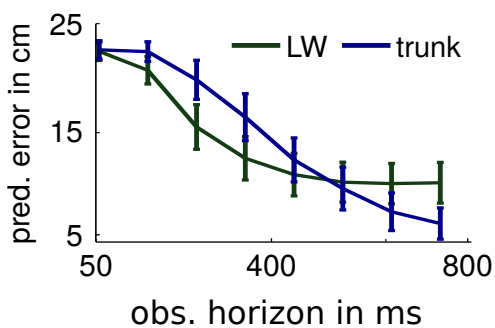


Figure 3.10: Supplementary figure, Trunk vs. Left Wrist prediction error: Average prediction error in cm over all subjects given the left wrist (LW) or the trunk motion as observation.

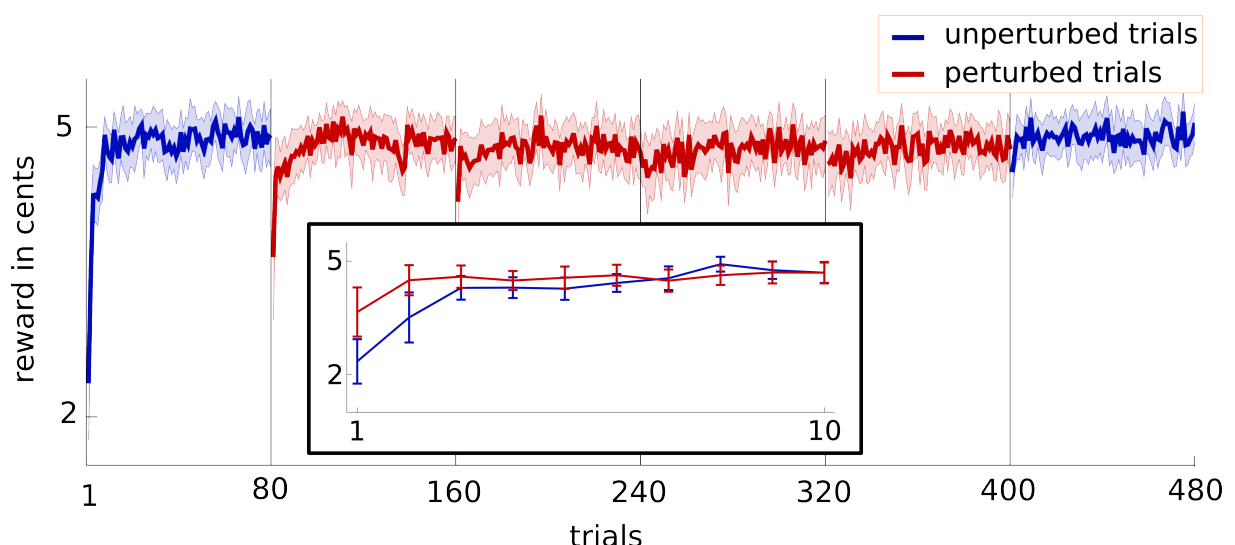


Figure 3.11: **Supplementary figure, Monetary rewards received:** Illustration of the received rewards averaged over all 20 subjects. The shaded region denotes the confidence bound.

Chapter 4

Use of rigid contacts during continuous perturbations

Standing balance in human everyday environment is often exposed to unpredictable and continuous external perturbations. Moreover, when postural control is impaired or challenged, handrails, canes, and handles are often used to assist maintaining balance and the effects of these firm supportive contacts in such conditions should be considered. Therefore, we examined changes in postural control in response to continuous, unpredictable perturbations and explored the effect of using a handle as a supportive contact. Postural control of standing subjects was assessed with measurements of centre of pressure (COP), which we also compared with perturbation waveform and forces exerted on the handle, to check for correlations. Kinematic data were used to determine changes in posture and electromyographic data to define the magnitude of muscle activity. The use of handle affected the control of posture by reducing the excursions of COP. The reduction was found to be more reflective in the posterior direction of COP excursions and was also in line with higher forces exerted on the handle in the same direction. The change of posture was immediate when the contact to the handle was omitted and significantly different between the two conditions. Muscle activation levels of the trunk flexor were significantly higher in the hand supported trial. In summary, we found that subjects clearly relied on using the handle for support, even though the perturbations did not pose a significant balance threat. Results of direction specific control of posture with hand support can be considered in rehabilitation and fall prevention programmes.

1 Introduction

Postural control is one of the vastly investigated area of human motor control in the last few decades. Most of the research on postural control focused on the role of sensory input in maintaining postural control during quiet standing, and in response to external balance perturbations. However, in our daily lives handrails, canes and handles are often used to assist maintaining balance, since they provide additional supportive contacts with the environment. With respect to the use of hand contacts for postural control, one of the most investigated phenomena is "light touch" [44, 50]. These light, fingertip contacts with stationary objects provide an additional sensory input, which helps individuals to better position them in space

[44]. Furthermore, a more accurate sensory information improves postural control by reducing the amplitude of the centre of pressure (COP) movement [44, 46, 49, 85]. However, hand contacts can serve as more than just sensory input. In situations where balance is exposed to larger perturbations, such as experienced on a moving bus or train, a firm hand contact (i.e. holding) is needed, as it provides a much better stabilising potential than a light touch [54]. Holding to a handle, besides increasing the base of support of a standing individual, also enables generation of forces at the hand to counteract such perturbations [68, 7]. For this, the location of the handle with respect to the subjects position is important. Babi et al. [7] recently found that handle position relative to the subject, along with support surface perturbation direction and intensity, has a significant effect on the maximal forces exerted at the handle during support surface perturbations in quiet standing. More specifically, lower forces exerted at handles located at shoulder and eye level were needed to maintain a comparable peak displacement of the COP. This indicates that handles were used for postural control irrespective of their position, but certain handle positions could be exploited more efficiently. Previously mentioned studies all based on discrete perturbations of balance. Such perturbations evoke reactive postural responses and conclusions were made on the basis of these responses. However, a major component of such responses is comprised of motor actions that are related to various sensorimotor reflexes and in less extent to the voluntary component of the postural control [13]. In contrast to discrete perturbations, continuous perturbations involve both reactive and proactive components of motor actions and in this sense offer a complementary insight into the postural control. Therefore, in this research we focused on changes in postural control during continuous perturbations of subject's balance. We aimed to record the mechanical function of the arm in a function of whole body balance stabilization to measure the effect of a firm hand contact on postural control.

2 Methods

We measured thirteen healthy right-handed young adults (average age = 22.2 years, SD = 2.2 years, average height 179 cm, SD = 6.2 cm and average weight = 76.7 kg, SD = 8.4 kg). The study was previously approved by the National medical ethics committee (No. 112/06/13) and all subjects participated after giving their written consent. Data of three subjects were excluded from the analyses due to some technical issues.

2.1 Experimental protocol

Subjects were standing on a force plate while their standing balance was being perturbed for 5 minutes by a motorized waist-pull system [61] (Fig 1). They were required to keep upright with their feet placed at hip width, look straight ahead, and maintain balance without making any unnecessary corrective steps. The experiment consisted of two conditions: balancing with ("with handle"; WH) and without ("no handle"; NH) holding onto a handle. In the WH condition subject held onto a stationary handle (diameter = 3.2 cm, length = 12 cm) positioned at shoulder height [7] with their right hand. In the NH condition subjects were standing freely with their arms folded across their chest. Balance was perturbed using a random white noise signal constructed to emulate mild, daily life perturbations (e.g., public transport) bus and

avoid large, abrupt, and startling balance perturbations. This perturbation signal was based on pilot experiments, had a frequency range between 0.25 and 1.00 Hz and the maximum perturbation force of 11% of the subject's body weight. Kinetic data were collected using a force plate (9281CA, Kistler Instrumente AG, Winterthur, Switzerland) under the subjects feet and a 3-axis force sensor (45E15A, JR3, Woodland, USA) on the base of the handle, both at 1000 samples/s. Unilateral (right hand side) kinematic data were collected at a sampling rate of 100 samples/s using a contactless motion capture system (3D Investigator, Northern Digital Inc., Waterloo, Ont., Canada) consisting of a 3×3 camera array. Seven active markers were attached on the subject's right 5th metatarsal-phalangeal, ankle, knee, hip, shoulder, elbow and wrist joint. Electromyographical (EMG) activity of the right leg (Tibialis Anterior; TA, Gastrocnemius lateralis: GA) and of the trunk (Multifidus; MF, Obliques Externus; OE) was measured using Biometrics DataLOG MW8X at a sampling rate of 1000 samples/s. Before the start of the experiment, subjects performed three maximal voluntary contractions (MVC) of each of the measured muscles and were exposed to 14 trials of 5 minutes of the WH condition. The aim of these preparatory WH trials was to familiarize the subjects with the experimental set-up and avoid any learning effects observed in previous balance experiments.

2.2 Data analysis

Anteroposterior displacement of the subjects centre of pressure (COP) was calculated from the data provided by the force plate on which the subjects were standing. Kinematic data were low pass filtered (zero lag, 2nd order Butterworth algorithm, cut-off frequency 20 Hz) [10] and ankle, knee, and hip joint angles were calculated from the joint markers coordinates. Mean values of joint angles over time were fitted using an exponential model $y = A e^{-t/\tau} + C$, where A is the gain of the exponential process, τ is the time constant, C is the offset, and t refers to the trial number) to describe evaluation of motor adaptation over time [31]. The onset of reaching a plateau (adaptation stabilized) was defined by calculating point in time at the three time constants (3τ) of the fitted exponential curve. This is the point when the function reaches a value of less than 5% of its starting value and was considered as the adaptation stabilized. EMG was band-pass filtered (zero lag, 2nd order Butterworth algorithm, with cut-off frequencies of 20 and 450 Hz), full-wave rectified and normalized by division with the MVCs. By applying a low pass filter (zero lag, 2nd order Butterworth algorithm, 10 Hz cut-off frequency), we created envelopes of EMG signals and then integrated them over time, to observe the accumulated EMG activity.

2.3 Statistical analysis

To compare the NH and WH conditions we calculated the average COP displacement, hip, knee, and ankle angles and contact forces exerted on the handle over the 5 minutes for each subject. These individual average values were used for statistical analysis. We used paired samples t-test analysis to investigate the differences between the WH and NH conditions and linear correlation to investigate the relationship between the COP displacement and the magnitude of the perturbation (separately for anterior and posterior directions) and between COP and the exerted handle contact force. All statistical analyses were performed using SPSS

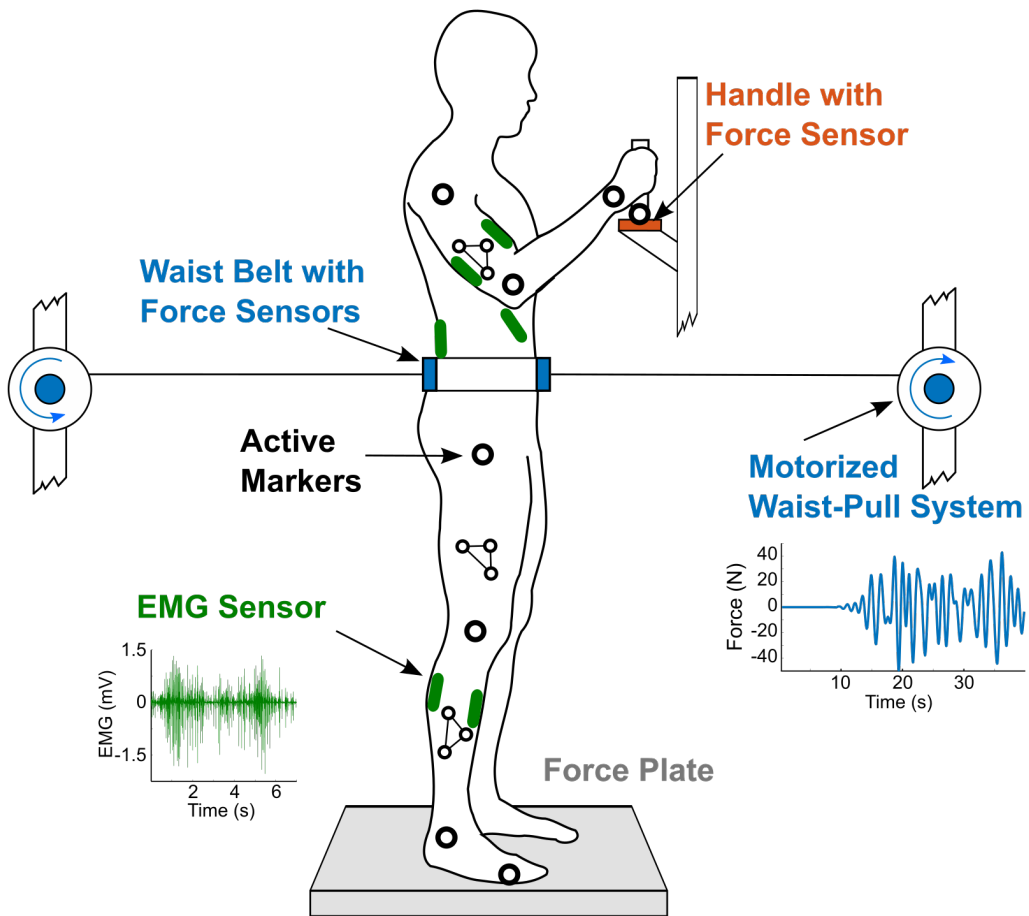


Figure 1: Experimental setup. The subject is standing on a force plate, wearing a waist belt connected to the motorized waist-pull system which generated translational force perturbations in the anterior-posterior direction using a random white noise signal constructed to emulate mild, daily life perturbations. The actual perturbation waveform is shown on the plot below the motorized waist-pull system.

21 Inc., Chicago, USA and statistical significance was set at $\alpha = 0.05$. The effect size (d) was calculated by using standard Cohens equation ($\hat{d} = \frac{\bar{X}_1 - \bar{X}_2}{s}$) [16].

After comparing the two trials we checked for direction specific differences of COP displacement within each trial. For this, we used a paired samples t-test on averaged measures of anteroposterior COP displacement. The relationship between the perturbation and the COP displacement was investigated in more detail by correlating the perturbation force and COP displacement and by correlating perturbation force and forces on the handle.

3 Results

Average anteroposterior displacements of the COP during the NH and WH conditions are shown in Fig 2. In both conditions COP displacement was larger in the anterior direction (mean \pm SE: NH 38.45 ± 1.6 mm, WH 18.15 ± 1.2 mm) compared to posterior (mean \pm

SE: NH -34.88 ± 2 mm, WH -11.02 ± 1.5 mm), but this difference was significant only for the WH condition ($t(9) = 2.81$, $p = .02$, $d = 1.52$). Hence, the remainder of our COP analyses were conducted for the anterior and posterior directions separately.

Overall, COP displacements were significantly larger in the NH condition compared to WH condition, both in the anterior (difference of 20.3 mm, $t(9) = 7.78$, $p = .001$, $d = -4.15$) and posterior direction (difference of 23.9 mm, $t(9) = -11.09$, $p = .001$, $d = -3.8$).

As can be seen from Fig 3A, the correlation between the COP displacement and perturbation force was $r_p = .77$ ($p < .001$) and $r_a = .82$ ($p < .001$) in the NH condition for the posterior and anterior direction, respectively. For the WH condition (Fig 3B) the correlations were $r_p = .67$ ($p < .001$) and $r_a = .89$ ($p < .001$) for the posterior and anterior direction, respectively.

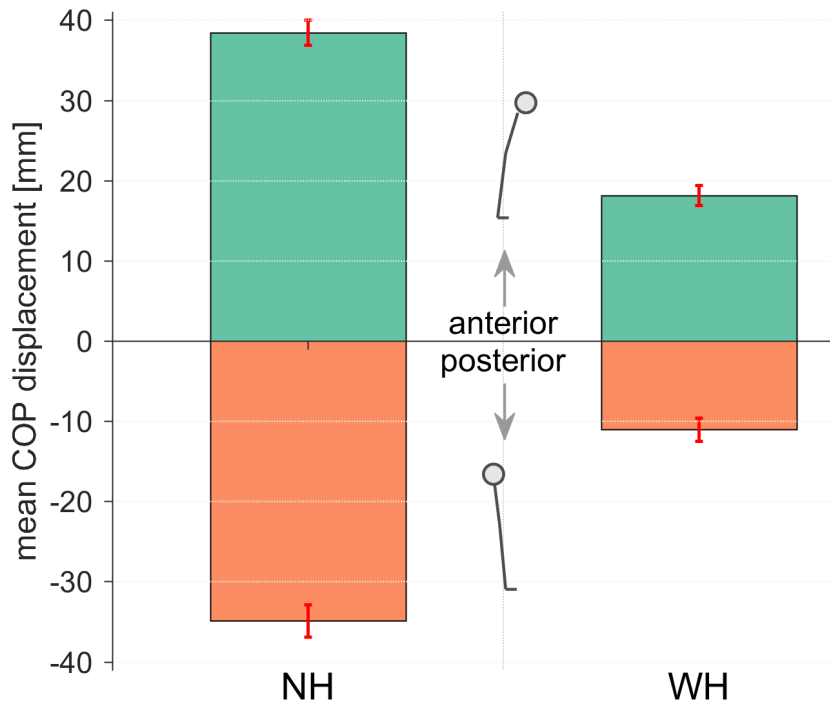


Figure 2: **Anteroposterior displacement of COP.** Mean COP displacement in NH and WH trials, for the anterior (positive) and posterior (negative) directions. Error bars indicate ± 1 standard error of the mean.

Correlations between the forces exerted on the handle and the perturbation force (Fig 3C) were large in both anterior ($r_p = .85$, $p < .001$) and posterior direction ($r_a = .81$, $p < .001$). However, the slope of a least-squares linear fit to the data indicates, that subjects utilized the handle considerably more for perturbations in the posterior direction ($k_p = 1.3$) than for perturbations in the anterior direction ($k_a = .86$).

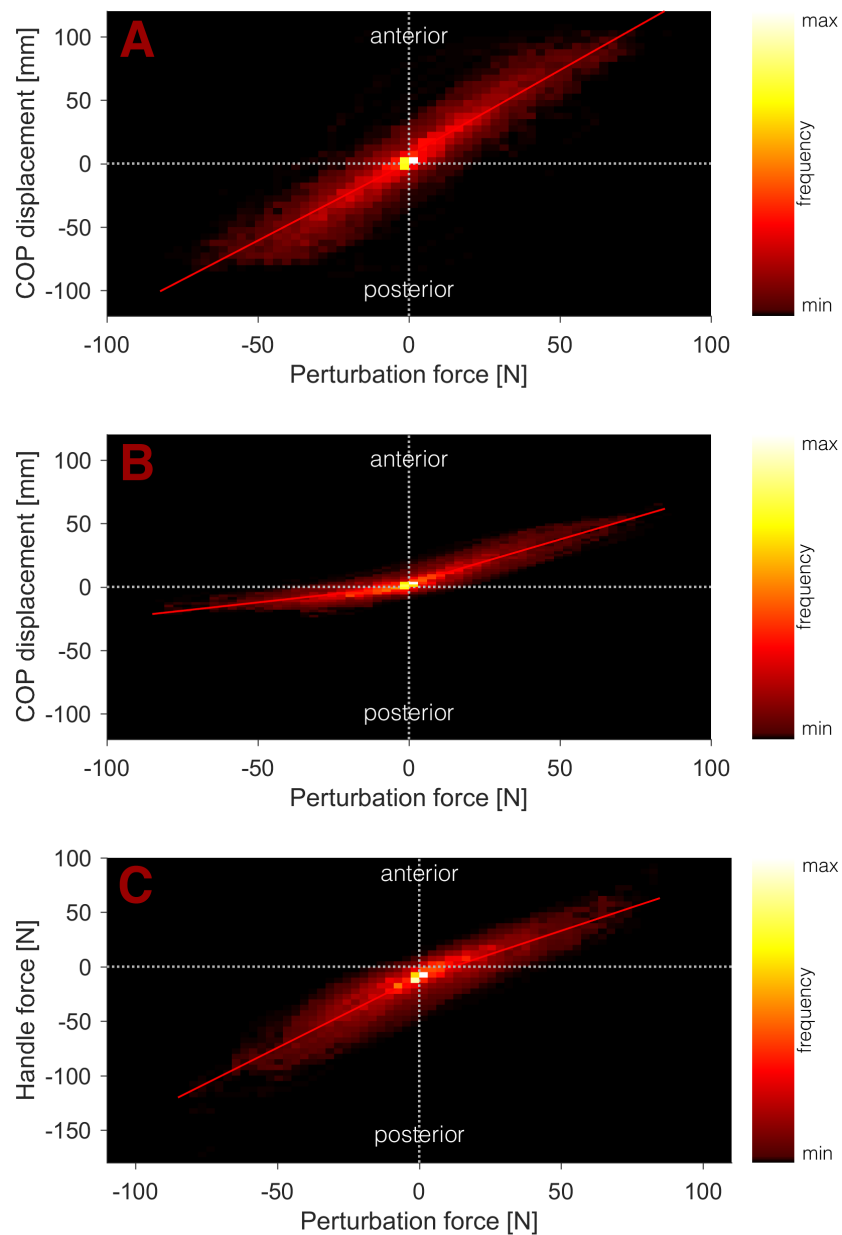


Figure 3: **Correlation.** **(A)** Correlation between the perturbation force and COP displacement in the NH condition, **(B)** correlation between COP displacement and perturbation force in the WH condition, and **(C)** correlation between handle force and perturbation force in the WH condition. All correlations were calculated separately for the anterior (positive) and posterior (negative) direction.

Joint angles prior to the start of perturbation were significantly smaller in the NH condition compared to WH condition (Fig 4). Differences were the largest in the knee (mean \pm SE: $169.4 \pm 1.4^\circ$ for NH, $172.9 \pm 1.4^\circ$ for WH, $t(9) = -4.05$, $p = .01$, $d = 1.36$), followed by the hip (mean \pm SE: $179 \pm 1.8^\circ$ for NH, $181.6 \pm 1.5^\circ$ WH, $t(9) = -2.95$, $p = .024$, $d = 1.13$), and ankle (mean \pm SE: $110.4 \pm 1.1^\circ$ for NH, $112.1 \pm 1.2^\circ$ WH, $t(9) = -2.71$, $p = .038$, $d = 1.08$).

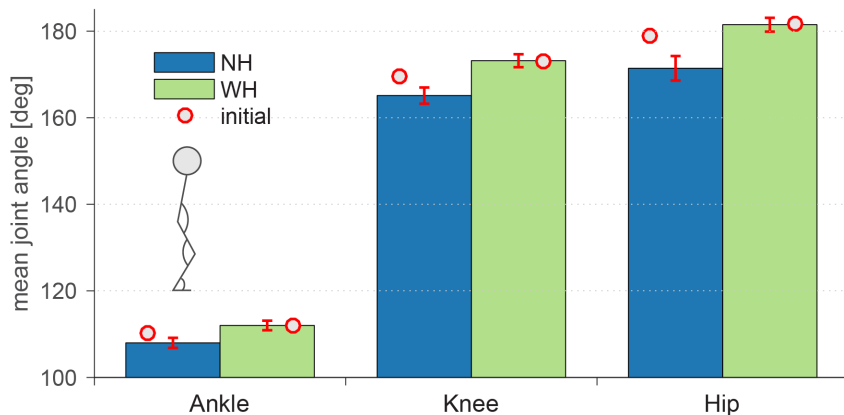


Figure 4: Ankle, knee and hip joint angles. Mean value of joint angles during the perturbation is given for NH (blue bars) and WH condition (green bars) and mean joint angles prior to the start of perturbation are shown as red circles above bars. Error bars indicate ± 1 standard error of the mean.

Ankle (A), knee (B), and hip (C) angles over the time course of the perturbation are shown in Fig 5. Exponential curves fitted to the data show that mean joint angles in the NH condition changed after the perturbation onset before reaching a steady state. The steady state was reached first by the ankle angle (86 s after perturbation onset), followed by the knee angle (112 s after the perturbation onset) and finally hip angle (195 s after the perturbation onset), resulting in more ankle, knee and hip flexion.

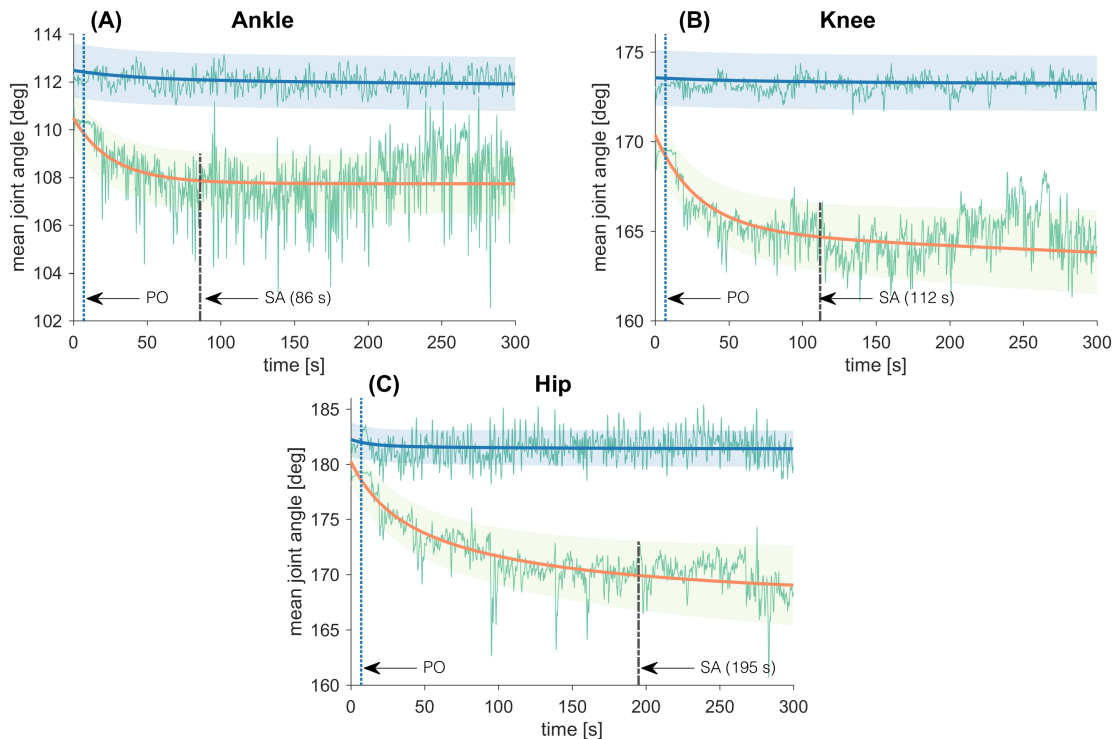


Figure 5: Ankle, knee and hip joint angles. Figures represent mean ankle (A), knee (B), and hip (C) angles over the time course of the perturbation. Thin solid curves represent mean joint angles during NH and WH conditions. Thick solid lines represent exponential curve fit, denoting adaptation of joint angles in the NH (orange) and WH (blue) conditions, while shaded areas represent standard error of the mean. The dotted vertical lines represent perturbation onset (PO) while the dashed vertical lines indicate stabilized changes (adaptation) in the joint angles (SA).

Finally, muscle activity is significantly lower during the WH condition than during the NH condition both for the leg muscles (GA $t(9) = 3.57, p = .04, d = -0.89$; TA $t(9) = 6.41, p = .002, d = -1.85$) and trunk muscle (MF $t(9) = 6.5, p = .001, d = -1.01$), as can be seen in Fig 6. Leg muscle activity is lower for $18.4 \pm 4.9\%$ in the GA (mean \pm SE: NH: $28.97 \pm 6.5\%$ MVC, WH: $10.6 \pm 2.3\%$ MVC) and for $23.7 \pm 3.5\%$ in the TA (mean \pm SE: NH: $27.21 \pm 4\%$ MVC, WH: $3.47 \pm 1.9\%$), while trunk muscle activity is lower for $14.3 \pm 2.1\%$ in the MF (mean \pm SE: NH: $36.17 \pm 4.5\%$ MVC, WH: $21.83 \pm 3.7\%$).

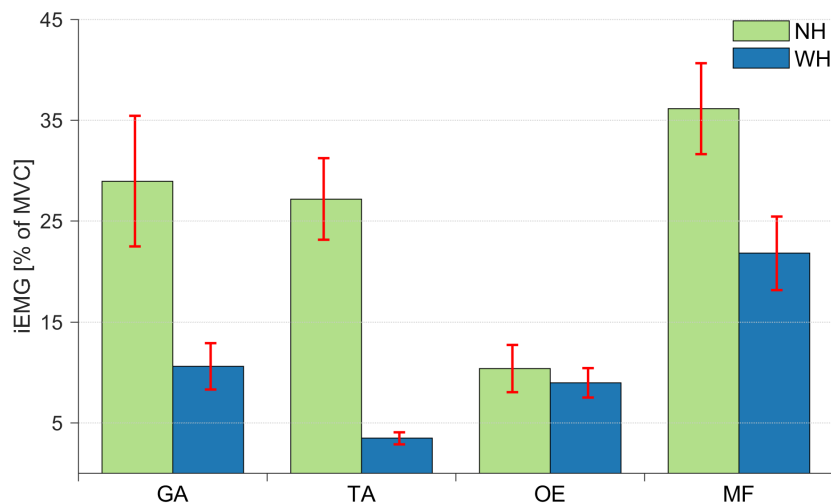


Figure 6: Muscle activity. Mean integrated EMG activity of leg (GA and TA) and trunk (OE and MF) muscles during the NH (green bars) and WH condition (blue bars). Error bars indicate ± 1 standard error of the mean.

4 Conclusions

Standing balance in human everyday environment is often exposed to unpredictable and continuous external perturbations. Moreover, when postural control is impaired or challenged, handrails, canes, and handles are often used to assist maintaining balance and the effects of these firm supportive contacts in such conditions should be considered. Therefore, we examined changes in postural control in response to continuous, unpredictable perturbations and explored the effect of using a handle as a supportive contact. Postural control of standing subjects was assessed with measurements of centre of pressure, which we also compared with perturbation waveform and forces exerted on the handle, to check for correlations. Kinematic data were used to determine changes in posture and electromyographic data to define the magnitude of muscle activity. COP displacement, hip, knee, and ankle angles, leg and trunk muscle activity and handle contact forces were analysed for the anterior and posterior directions separately, as COP displacement was significantly larger in the anterior direction (WH, 7 mm, $p = .02$). Perturbation force was strongly correlated to COP displacement (all $r > .65$) and handle forces ($r > .8$) in both directions. COP displacement was significantly larger in the NH condition compared to WH condition (anterior: 20 mm, posterior: 24 mm, both p

= .001) and regression indicated that subjects utilized the handle slightly more for posterior perturbations. In the NH condition, all joint angles decreased in anticipation of the perturbation (2-4°, all $p < .04$) and until 86-195 s following perturbation onset. Finally, leg (18-24%) and one of the trunk (14%) muscles increased their activity in the NH condition (all $p \leq .04$). In summary, we found that subjects clearly relied on using the handle for support, even though the perturbations did not pose a significant balance threat. Results of direction specific control of posture with hand support can be considered in rehabilitation and fall prevention programs.

Chapter 5

Learning compliant contacts

A pilot study aims at examining how humans learn compliant force dynamics and modulate their whole-body motions to reach anticipated goals. Here, we present an experimental idea to measure the goal-directed movements against compliant forces, and then illustrate the ongoing results which were conducted for a few human subjects. At this pilot stage, we are focusing on the simple linear compliant case and discuss further experiments. To deepen understanding of the mechanism in humans, it would be beneficial to develop the humanoid robot control in interacting with multiple compliant surfaces.

1 Introduction

Humans can learn how to control their own body movements in an uncertain environment, and utilise it to predict the consequences of actions and to achieve a behavioural goal [?, ?]. A considerable amount of research has shown the human capabilities of generalization in visuo-motor learning and has been exploring the underlying mechanisms [?, ?]. A certain exposure to a new physical environment facilitates to generalize the spatial and temporal characteristics of the point-to-point movements via error-based learning and perturbation paradigm. In the real-world interactions, there are varied and complicated force dynamics (i.e., governed by not only simple linear principles) when making a contact with an object and handling it. The optimal functions seem to be perceptually learned via repetitive movements against the force. However, to our knowledge, little is still known about how humans can generalize the compliant force dynamics itself and utilize it to their future motor plan.

The CoDyCo project has been investigating the whole-body coordination mechanisms in arm reaching movements and the postural balance control in assistive contact with rigid and/or compliant surfaces. Like humans, robots are required to flexibly adjust their posture and to coordinate the physical mobility with augmented autonomy. We expect that humans could generalize the force principles in a cognitively robust way via force-feedback from the early stage of the body movements. To explore the generalization mechanism of the force dynamics in humans and to model it would provide a useful strategy in humanoid robot control. The successful model could be exploited to effectively control autonomous robots' whole-body balance in interacting with the environment through supportive contacts.

In a pilot study, we focused on a simple case: linear compliant force. We employed a haptic device, Haptic Master (Moog, Inc.), which is controlled by a set of a computer programmes

to render robotic manipulandum for force feedback. The pilot experiment measured the end-effector movements controlled by human subjects and analysed the dynamic properties of the movements against the compliant force and the performance.

2 Methods

2.1 Modelling

In general, spring-damper force (\mathbf{F}) is formulated by the position and the velocity with parameters: spring stiffness (k) and spring damping factor (λ). Here, it is simplified for one direction (Z).

$$\mathbf{F} = kZ^n + (\lambda Z^p) \dot{Z}. \quad (1)$$

We employed the ready-made spring model in the Haptic API, where the compliant force formula was assigned to the device, the Haptic Master. The compliant force was rendered by the end-effector position and the velocity with the parameters in real-time (Fig. 1).

2.2 Experimental Design

As a pilot study, we employed a simple linear spring-damper formula:

$$\mathbf{F} = kZ + \lambda \dot{Z}. \quad (2)$$

The compliant force formula is assigned to the model in the Haptic Master. Aiming to simplify analysing the performance, the forces and the movements were constrained in the only one direction, here, in the vertical (Z) direction to the ground.

Human subjects learned a spring compliant force via repetitive reaching movements to the first target ($z = t_1$) in a certain period of time, - so called “Learning session”. Then, they were asked to move the end-effector to the second, or test, target ($z = t_2$), which was set more far from the t_1 position, as a test trial; so, more force would be required for this movement (Fig.2). In order to achieve the t_2 target, the participants would exploit their prior knowledge of the force dynamics experienced via learning session. We will evaluate whether and how the motion performance is likely to follow the formula previously learned.

2.3 Apparatus and Stimuli

The haptic device, “Haptic Master” consisted of a large robotic rod with an end-effector. The “Home” position, where the centre of the end effector is $z = 0$ at the workspace, was 110 cm from the ground. The spring position was set at $z = 0$. In this study, the rod movements were restricted in the vertical direction only.

The visual information about the task was provided at the computer display to human subjects. The computer screen was located at the right side of the Haptic Master from the subjects; where the centre of the screen was approximately 80 cm from the centre of the robotic rod. The screen was approximately 1 m away from the participants’ standpoint, and 80 cm away from the centre of the end effector position. The screen displayed the target position and the end-effector position in real-time (Fig. 3). The target positions were set at $z = t_1$ (50 mm for learning), and $z = t_2$ (100 mm for test).

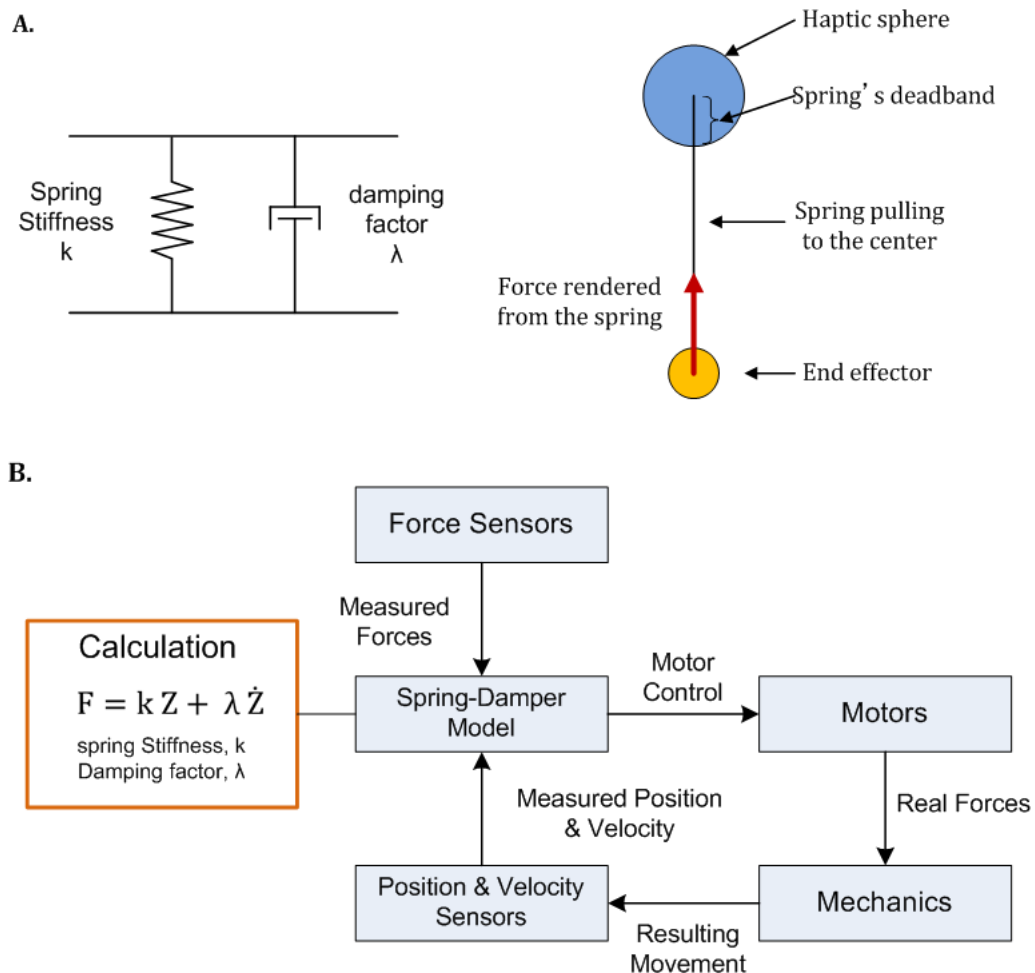


Figure 1: A. The ready-made spring model in the Haptic API. B. Block diagram of the compliant force control. The force is rendering based on the end-effector position and the velocity with parameters (spring stiffness and damping factors) in the real time.

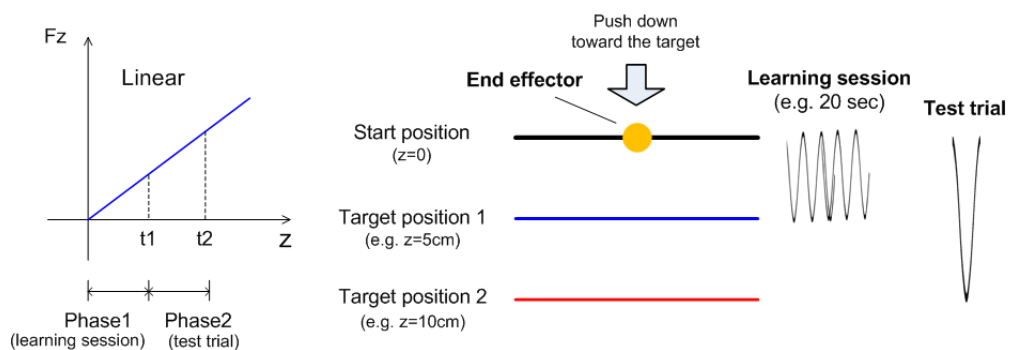


Figure 2: Experimental Design. Two target positions were set: $z = t_1$ for learning session and $z = t_2$ for test trial.

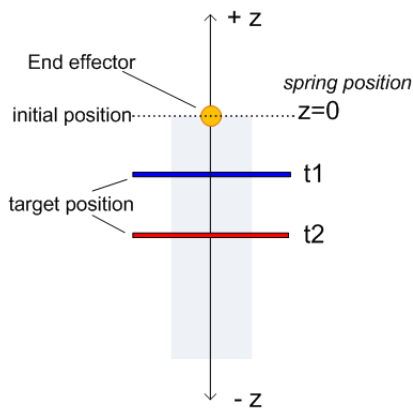


Figure 3: Experimental visual stimuli. The end-effector and the two target positions ($z = t_1$ and $z = t_2$) were visually indicated on the computer screen.

2.4 Procedure and analyses

Participants stood in front of the haptic device and grasped the end-effector. Firstly, they conducted a practice session followed by the main blocks. They were required to make repetitive movements against compliant force generated by the device to learn the kinetic principle. The movements were monitored by visual information on the screen. Participants pushed the end-effector to reach the target position, and then released the end-effector to allow it to freely return to the initial position ($z=0$). They were asked to set the centre of the end-effector position on the target as accurate as possible.

The main block consisted of two parts: Learning session and Test trial. In the Learning session, the target position was set at $z = t_1$, described above. Participants controlled the end-effector by their own timing, or rhythm, per each movement in the current pilot study (the specific time windows were not set up by the programme for the series of movements: i.e., push the end-effector down from the start position and reach the target position). The visual feedback was given when the end-effector reached to the target; the target colour indicated this by changing from blue to yellow. Participants learnt the compliant force dynamics by the repetitive movements. The experimenter monitored the elapsed time using a stopwatch, and verbally informed the end of the session when 20 seconds passed. Participant stopped their repetitive movements immediately and prepared for the trial session.

In the Test trial, participants moved the end-effector to the target (coloured red line, $z = t_2$) three times based on the formula they previously learned. In this phase, no visual feedback in the relationship between the end-effector position and the target was given to the subjects.

One block consists of three sets (Learning session + Test trial). Participants conducted three blocks; so, 3 blocks in total, and 9 test trials. Under the current settings, the experiment was completed within approximately 20 minutes on average.

The dynamic properties of the point-to-point movements were measured: the end-effector's position (Z), the velocity (\dot{Z}), and the force (F_Z) across the time. These were recorded by the 20 msec sampling rate properties were analysed and compared between the linear and the non-linear force conditions.

3 Results and Discussions

3.1 Participants

Six male subjects (age: 28.8 +/- 3.1 (SD), height: 175.3 cm +/- 7.1 (SD), weight: 79.5 kg +/- 17.8 (SD), one left-handed) voluntarily participated in the pilot experiment. All had normal or corrected to normal vision, and they had no known motor deficits and/or any limb injuries (self-reported). They were recruited from the student and staff population at University of Birmingham. (One was not nave to the purpose of the experiment.)

3.2 Ongoing Results

The end-effector position, velocity and force were recorded. Here, illustrates the one participant's one block performance, as an example (Fig 4).

In order to examine the each reaching movement, the data were extracted from the total between the start ($z = 0.01\text{m}$) and the end (approx. $z = t_2$) positions, where the end-effector was released to return to the initial position. These points were determined by calculating the each inflection point (Fig 5).

The data were averaged across three blocks; one block consisted of three (Learning + Trial) sessions; so participants ideally completed 9 sessions in total, but one (subj.03) accidentally completed only two blocks because of the setting errors. The averaged numbers of repetitions were $152.8 +/- 45.6$ (SD) in the Learning session and $27.2 +/- 6.1$ (SD) in the Test trial. All six participants' averaged data (the end-effector position, velocity and force) can be seen from Fig.6 to Fig. 8.

3.3 Brief Discussion

The Fig 9 showed that some participants (e.g., Subj.01, Subj.06) performed to reach the target position ($z = t_2$) much faster than the expected time duration, which was estimated from the linear equation. That is, the t_2 position was double distance of the t_1 from the start position; so the reaching time would be estimated close to the double. The time would not be able to calculate by the simple linear calculation because the damping factor depends on the velocity, though.

This might be caused by the experimental design; that is, participants made the repetitive movements with their own rhythms at the learning session. Because they tend to keep their rhythms even in the consecutive trial session, and then they might have unconsciously increased the force or accelerated their speed to reach the target. This possibility can be seen at their movement profiles (Fig.7: velocity and Fig.8: force). Several studies have shown that time perception plays an important role in human motor control [?, ?]; therefore, this timing issue should be carefully considered into the experimental design and should avoid any confounding factors. To do this, we will visually guide the participants' movements with a certain time-windows in the future experiment.

Moreover, in the current pilot experiment, the judgment of reaching the target was inaccurate. Although the participants received the visual feedback at the learning session, it only indicated the end-effector crossed the target position, and also there were no task reward.

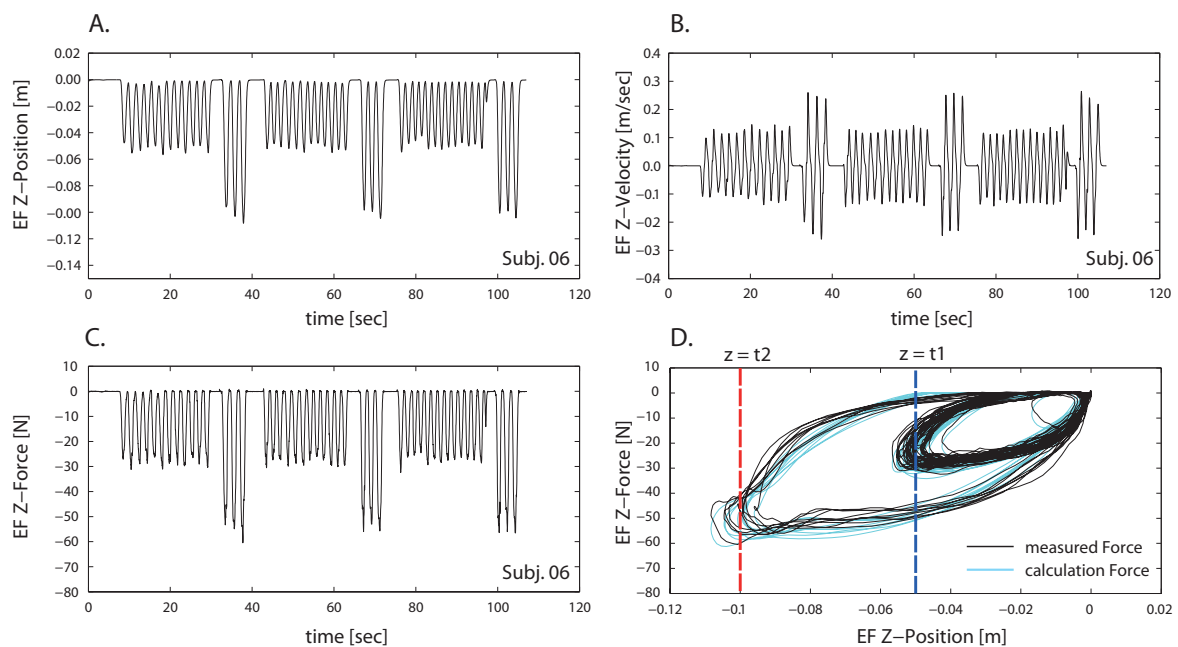


Figure 4: The total recording of the completion of the first block. (Subj. 06). **A.** End-effector Z-position, **B.** Z-velocity and **C.** Z-force. **D.** the relationship between the position and the force compared between the force directly measured by the sensor and the force calculated by the equation with the real time z-position and z-velocity.

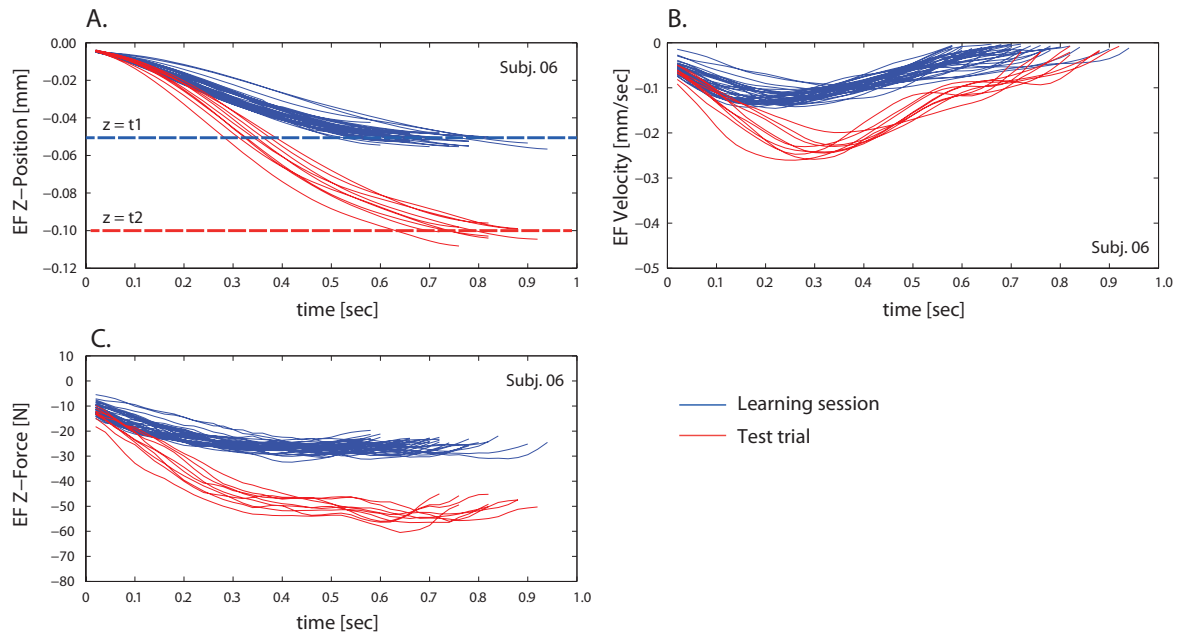


Figure 5: Experimental data for one participant (the first block, three test trials). Red lines represent the forces, which were directly measured by a sensor at the end-effector. Blue lines represent the forces, which were calculated in the real time by spring stiffness and damping factor with the end-effector position.

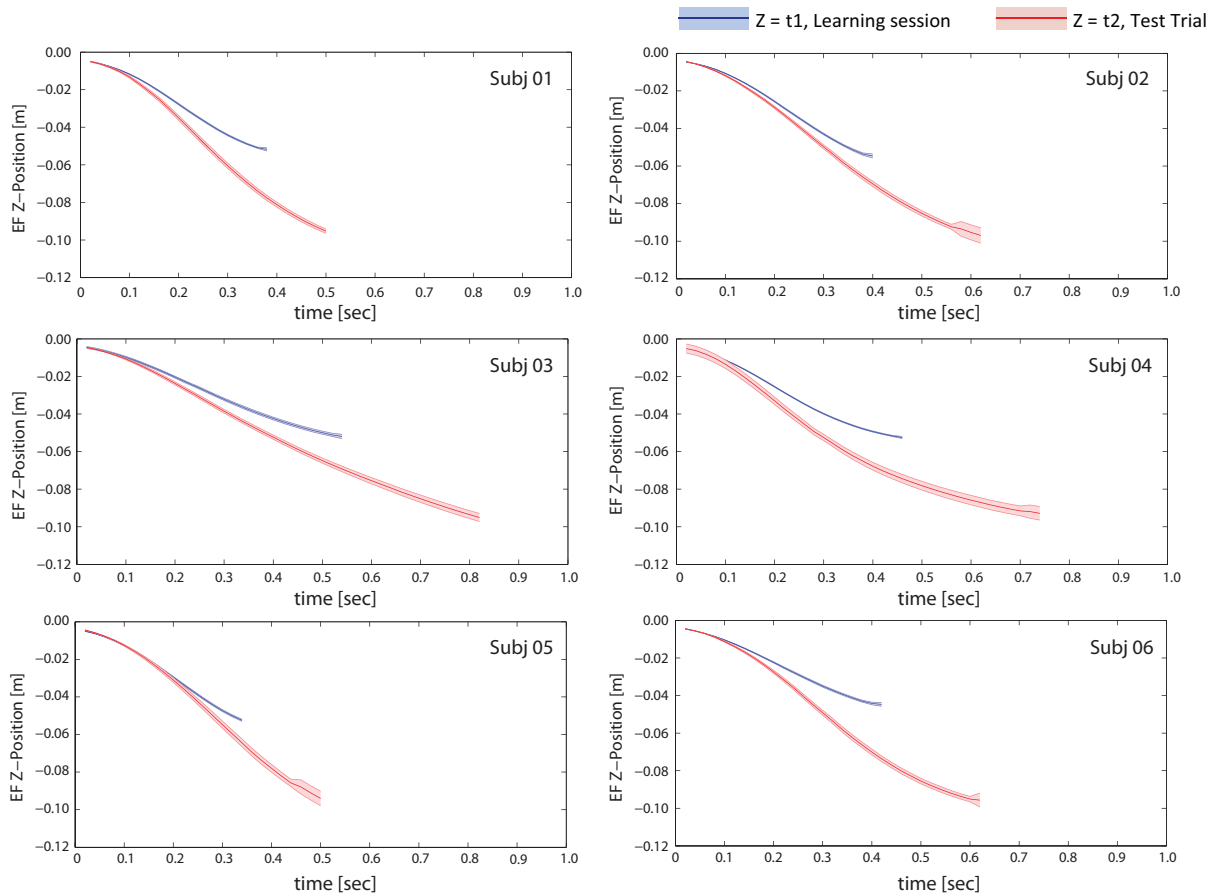


Figure 6: The averaged end-effector z-position performance in the reaching movements against the linear spring-damper force for 6 subjects. The data were averaged across 3 blocks (9 (Learning + Trial) sessions). The blue lines represent the average performance in the Learning session, and the red in the Test trial, the coloured areas represent their standard error respectively.

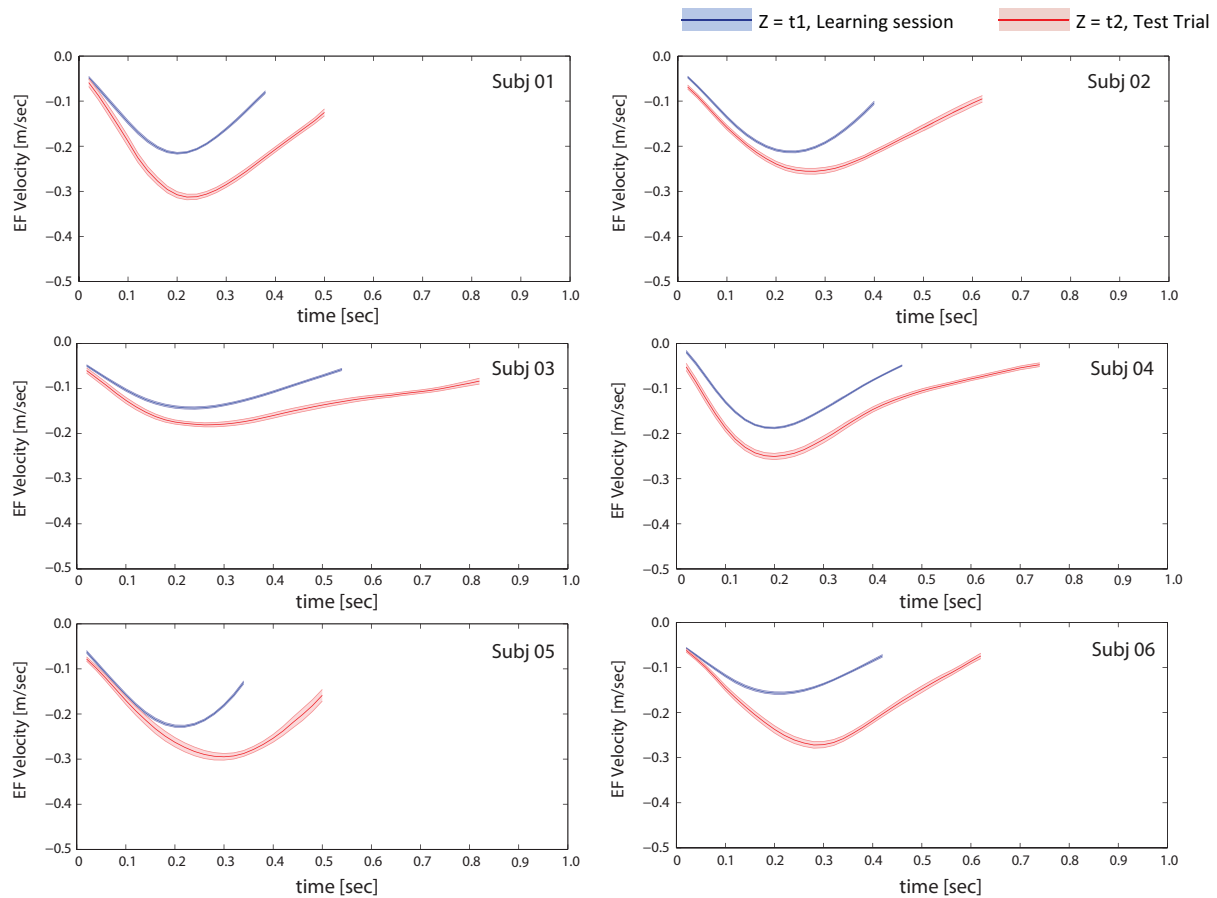


Figure 7: The averaged end-effector z-velocity performance in the reaching movements against the linear spring-damper force for 6 subjects. The data were averaged across 3 blocks (9 (Learning + Trial) sessions). The blue lines represent the average performance in the Learning session, and the red in the Test trial, the coloured areas represent their standard error respectively.

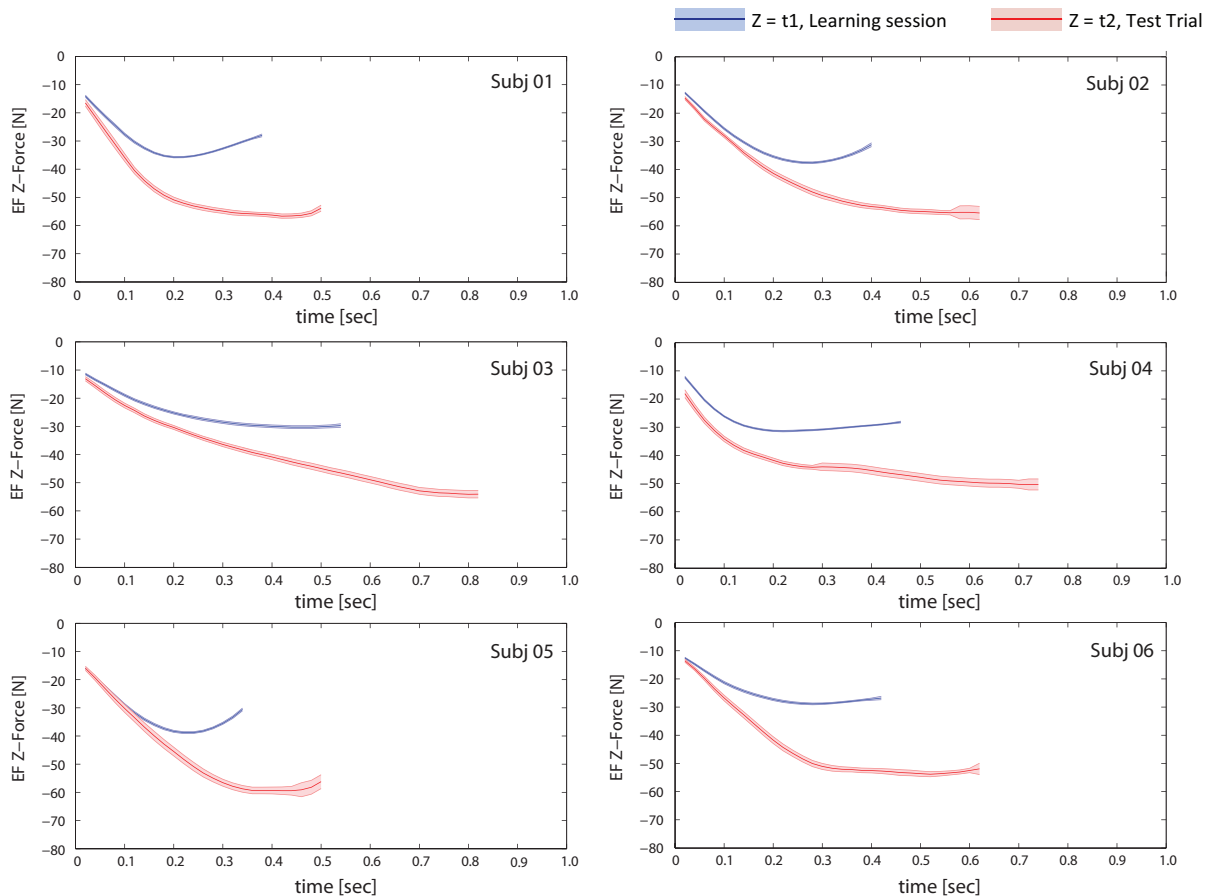


Figure 8: The averaged end-effector z-force performance in the reaching movements against the linear spring-damper force for 6 subjects. The data were averaged across 3 blocks (9 (Learning + Trial) sessions). The blue lines represent the average performance in the Learning session, and the red in the Test trial, the coloured areas represent their standard error respectively.

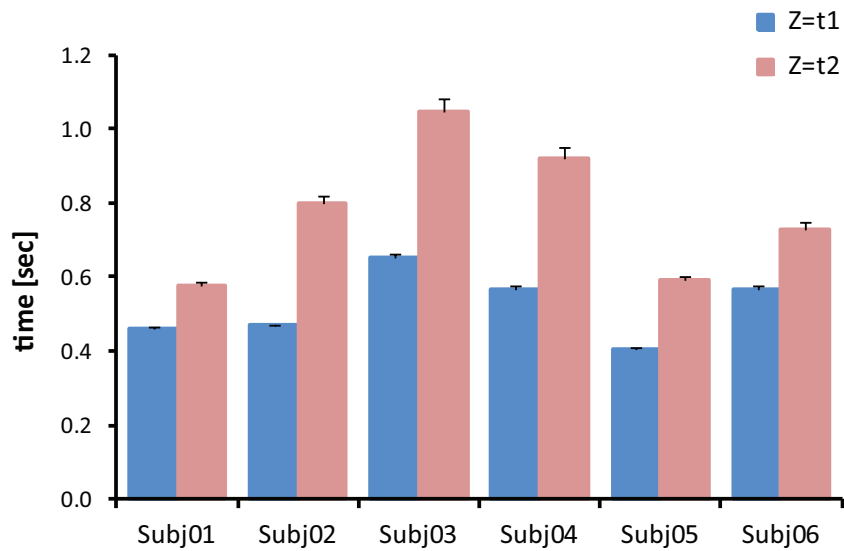


Figure 9: Illustrate averaged time to reach the targets with the comparison between the Learning session (blue) and the Test trial (red) for six subjects. The error bars represents the standard error across the total number of the repetitions.

The inaccuracy would have affected their force perception and movements [?] therefore, in the next experiment, we will set a specific correct zone visually defined by a more accurate way (e.g. the similar size of sphere of the end-effector) as the target instead of the line indicators. The task completion in the Learning session would be determined by their performance and individual learning level would be evaluated by their correct movements.

The current analyses conducted for all performance in the test trial (reaching the target ($z = t_2$) three times for each), but the performance might have needed to be evaluated focusing on the first trial only, because the first movement was directly affected by the learning session and the second and the third movements were gradually contaminated.

Overall, through the pilot experiment, we have learned the importance of the timing issue in interacting with compliant surface. We will improve the experimental design and strictly control the parameters (timing, speed, and the accuracy).

In the future experiment, based on the linear case, we will measure the pattern under the non-linear compliant forces and examine the human goal-directed performance. Besides, as well as the spring-damper, it may help the understanding of the generalization if we employ another compliant force model (e.g. object surface).

Bibliography

- [1] Whole-body compliant dynamical contacts in cognitive humanoids. <https://www.codyco.eu>. Accessed: 2015-10-20.
- [2] K Adolph. Learning to keep balance. *Advances in child development and behavior*, 30:1–40, 2002.
- [3] Karen E Adolph and Sarah E Berger. Motor development. *Handbook of child psychology*, 2006.
- [4] Dennis E. Anderson, Michael L. Madigan, and Maury A. Nussbaum. Maximum voluntary joint torque as a function of joint angle and angular velocity: model development and application to the lower limb. *Journal of biomechanics*, 40(14):3105–13, jan 2007.
- [5] Christopher G Atkeson and Benjamin Stephens. Multiple balance strategies from one optimization criterion. 2007.
- [6] Jan Babič, Tadej Petrič, Luka Peternel, and Nejc Šarabon. Effects of supportive hand contact on reactive postural control during support perturbations. *Gait & posture*, 40(3):441–446, 2014.
- [7] Jan Babič, Tadej Petrič, Luka Peternel, and Nejc Šarabon. Effects of supportive hand contact on reactive postural control during support perturbations. *Gait and Posture*, 40(3):441–446, jun 2014.
- [8] J Babič, T Petrič, L Peternel, and N Šarabon. Effects of supportive hand contact on reactive postural control during support perturbations. *Gait and Posture*, 40(3):441–446, 2014.
- [9] Ramesh Balasubramaniam and Alan M Wing. The dynamics of standing balance. *Trends in cognitive sciences*, 6(12):531–536, 2002.
- [10] Roger Bartlett. *Introduction to Sports Biomechanics: Analysing Human Movement Patterns*. Routledge, Abingdon, UK, 2 edition, 2007.
- [11] Denise J Berger, Reinhard Gentner, Timothy Edmunds, Dinesh K Pai, and Andrea d’Avella. Differences in adaptation rates after virtual surgeries provide direct evidence for modularity. *The Journal of Neuroscience*, 33(30):12384–12394, 2013.
- [12] Martin Bland et al. *An introduction to medical statistics*. Number Ed. 3. Oxford University Press, 2000.

- [13] Tadeusz Bober, Kornelia Kulig, and Judith M Burnfield. Predictive torque equations for joints of the extremities. *Acta of Bioengineering and Biomechanics*, 4(2):49–61, 2002.
- [14] S Bouisset and M Zattara. A sequence of postural movements precedes voluntary movement. *Neuroscience letters*, 22(3):263–270, 1981.
- [15] A Bowling and O Khatib. The dynamic capability equations: a new tool for analyzing robotic manipulator performance. *IEEE Trans. Robotics*, 21(1):115–123, Feb 2005.
- [16] Jacob Cohen. *Statistical Power Analysis for the Behavioral Sciences*. Lawrence Erlbaum Associates, 2 edition, 1988.
- [17] PJ Cordo and LEWIS M Nashner. Properties of postural adjustments associated with rapid arm movements. *Journal of neurophysiology*, 47(2):287–302, 1982.
- [18] S Cotton, P Fraisse, and A Murray. On the manipulability of the center of mass of humanoid robots, application to design.
- [19] Andrea d'Avella, Alessandro Portone, Laure Fernandez, and Francesco Lacquaniti. Control of fast-reaching movements by muscle synergy combinations. *The Journal of neuroscience*, 26(30):7791–7810, 2006.
- [20] A. Dempster, N. Laird, and D. Rubin. Maximum likelihood from incomplete data via the EM algorithm. *Journal of the Royal Statistical Society, Series B*, 39(1):1–38, 1977.
- [21] R Dickstein, RJ Peterka, and FB Horak. Effects of light fingertip touch on postural responses in subjects with diabetic neuropathy. *Journal of Neurology, Neurosurgery & Psychiatry*, 74(5):620–626, 2003.
- [22] Jörn Diedrichsen, Reza Shadmehr, and Richard B Ivry. The coordination of movement: optimal feedback control and beyond. *Trends in cognitive sciences*, 14(1):31–39, 2010.
- [23] K Doty, C Melchiorri, and C Bonivento. A theory of generalized inverses applied to robotics. *Int. J. Robotics Research*, 12(1):1–19, Feb 1993.
- [24] K Doty, C Melchiorri, E Schwartz, and C Bonivento. Robot manipulability. *IEEE Trans. Robotics and Automation*, 11(3):462–468, June 1995.
- [25] Pamela W Duncan, Debra K Weiner, Julie Chandler, and Stephanie Studenski. Functional reach: a new clinical measure of balance. *Journal of gerontology*, 45(6):M192–M197, 1990.
- [26] R Featherstone. Spatialv2: Matlab toolbox.
- [27] R Featherstone. *Rigid body dynamics algorithms*. Springer, 2008.
- [28] R Featherstone. Analysis and design of planar self-balancing double-pendulum robots. In *19th Symposium on Robot Design, Dynamics and Control (RoManSy)*, pages 259–266, Paris, France, 2012.

- [29] R Featherstone. Quantitative measures of a robot's ability to balance. In *Int. Conf. Robotics Science & Systems*, Rome, Italy, 2015.
- [30] T Flash and F Mussa-Ivaldi. Human arm stiffness characteristics during the maintenance of posture. *Experimental brain research*, 82(2):315–326, 1990.
- [31] David W Franklin, Rieko Osu, Etienne Burdet, Mitsuo Kawato, and Theodore E Milner. Adaptation to stable and unstable dynamics achieved by combined impedance control and inverse dynamics model. *Journal of neurophysiology*, 90(5):3270–3282, 2003.
- [32] S. C. Gandevia, R. D. Herbert, and J. B. Leeper. Voluntary activation of human elbow flexor muscles during maximal concentric contractions. *Journal of Physiology*, 512(2):595–602, 1998.
- [33] S Gard, S Miff, and A Kuo. Comparison of kinematic and kinetic methods for computing the vertical motion of the body center of mass during walking. *J. Human Movement Science*, 22(6):597–610, 2004.
- [34] A Goswami. Foot rotation indicator (fri) point: a new gait planning tool to evaluate postural stability of biped robots. In *IEEE Int. Conf. Robotics and Automation*, pages 47–52, 1999.
- [35] A Goswami and V Kallem. Rate of change of angular momentum and balance maintenance of biped robots. In *IEEE Int. Conf. Robotics and Automation*, pages 3785–3790, New Orleans, LA, 2004.
- [36] Y Gu, C Lee, and B Yao. Feasible center of mass dynamic manipulability of humanoid robots. In *IEEE Int. Conf. Robotics and Automation*, pages 5082–5087, Seattle, Washington, May 2015.
- [37] L Guilamo, J Kuffner, K Nishiwaki, and S Kagami. Manipulability optimization for trajectory generation. In *IEEE Int. Conf. Robotics and Automation*, pages 2017–2022, Orlando, Florida, May 2006.
- [38] J Hermens, B Freriks, R Merletti, D Stegeman, J Blok, G Rau, C Disselhorst-Klug, and G Hagg. European recommendations for surface electromyography: Results of the seniam project (seniam). *Enschede*, 1999.
- [39] F Horak and L Nashner. *J. Neurophysiology*, 55(6):1369–1381, 1986.
- [40] Fay B Horak and Lewis M Nashner. Central programming of postural movements: adaptation to altered support-surface configurations. *Journal of neurophysiology*, 55(6):1369–1381, 1986.
- [41] R Huys, A Daffertshofer, and P J Beek. Multiple time scales and multiform dynamics in learning to juggle. *Motor Control*, 8:188–212, 2004.
- [42] Sang-Ho Hyon, Joshua G Hale, and Gordon Cheng. Full-body compliant human–humanoid interaction: balancing in the presence of unknown external forces. *Robotics, IEEE Transactions on*, 23(5):884–898, 2007.

- [43] Auke Jan Ijspeert, Jun Nakanishi, Heiko Hoffmann, Peter Pastor, and Stefan Schaal. Dynamical movement primitives: learning attractor models for motor behaviors. *Neural computation*, 25(2):328–373, 2013.
- [44] John J Jeka. Light touch contact as a balance aid. *Physical therapy*, 77(5):476–87, may 1997.
- [45] John J Jeka and James R Lackner. Fingertip contact influences human postural control. *Experimental Brain Research*, 79(2):495–502, 1994.
- [46] Leif Johannsen, Alan M Wing, and Vassilia Hatzitaki. Effects of maintaining touch contact on predictive and reactive balance. *Journal of neurophysiology*, 97(4):2686–2695, 2007.
- [47] Roberta L Klatzky, Thomas G Fikes, and James W Pellegrino. Planning for hand shape and arm transport when reaching for objects. *Acta Psychologica*, 88(3):209–232, 1995.
- [48] H Klove. Clinical neuropsychology. *The medical clinics of North America*, 47:1647–1658, 1963.
- [49] Motoki Kouzaki and Kei Masani. Reduced postural sway during quiet standing by light touch is due to finger tactile feedback but not mechanical support. *Experimental Brain Research*, 188(1):153–158, 2008.
- [50] Vijaya Krishnamoorthy, Harm Slijper, and Mark L. Latash. Effects of different types of light touch on postural sway. *Experimental Brain Research*, 147(1):71–79, 2002.
- [51] Arthur D Kuo. An optimal control model for analyzing human postural balance. *Biomedical Engineering, IEEE Transactions on*, 42(1):87–101, 1995.
- [52] Daniel B. Lockhart and Lena H. Ting. Optimal sensorimotor transformations for balance. *Nature Neuroscience*, 10(10):1329–1336, October 2007.
- [53] B Maki and McIlroy W. The role of limb movements in maintaining upright stance: the change-in-support strategy. *Physical Therapy*, 77(5):488–507, 1997.
- [54] Brian E Maki and William E McIlroy. The role of limb movements in maintaining upright stance: the "change-in-support" strategy. *Physical therapy*, 77(5):488–507, may 1997.
- [55] T Mergner. A neurological view on reactive human stance control. *Annual Reviews in Control*, 34(2):177–198, 2010.
- [56] Nancy J Minschew, KiBum Sung, Bobby L Jones, and Joseph M Furman. Underdevelopment of the postural control system in autism. *Neurology*, 63(11):2056–2061, 2004.
- [57] Amélie Moraux, Aurélie Canal, Gwenn Ollivier, Isabelle Ledoux, Valérie Doppler, Christine Payan, and Jean-Yves Hogrel. Ankle dorsi- and plantar-flexion torques measured by dynamometry in healthy subjects from 5 to 80 years. *BMC musculoskeletal disorders*, 14:104, 2013.

- [58] N Naksuk and C Lee. Zero moment point manipulability ellipsoid. In *IEEE Int. Conf. Robotics and Automation*, pages 1970–1975, Orlando, Florida, May 2006.
- [59] Yi-Chung Pai and James Patton. Center of mass velocity-position predictions for balance control. *Journal of biomechanics*, 30(4):347–354, 1997.
- [60] L Peternel and J Babič. Learning of compliant human-robot interaction using full-body haptic interface. *J. Advanced Robotics*, 27(13):003–1012, June 2013.
- [61] Luka Peternel and Jan Babič. Learning of compliant human-robot interaction using full-body haptic interface. *Advanced Robotics*, 27(13):1003–1012, sep 2013.
- [62] D Prattichizzo, M Malvezzi, M Gabiccini, and A Bicchi. On the manipulability ellipsoids of underactuated robotic hands with compliance. *Robotics and Autonomous Systems*, 60(3):337–346, March 2012.
- [63] Edward S Reed. An outline of a theory of action systems. *Journal of motor behavior*, 14(2):98–134, 1982.
- [64] E. Rueckert, J. Mundo, A. Paraschos, J. Peters, and G. Neumann. Extracting low-dimensional control variables for movement primitives. In *Proceedings of the International Conference on Robotics and Automation (ICRA)*, 2015.
- [65] Elmar Rueckert and Andrea d’Avella. Learned parametrized dynamic movement primitives with shared synergies for controlling robotic and musculoskeletal systems. *Frontiers in Computational Neuroscience (Special Issue on Modularity in motor control: from muscle synergies to cognitive action representation)*, 7(138), 2013.
- [66] Elmar Rueckert, Max Mindt, Jan Peters, and Gerhard Neumann. Robust policy updates for stochastic optimal control. In *Humanoid Robots (Humanoids), 2014 14th IEEE-RAS International Conference on*, pages 388–393. IEEE, 2014.
- [67] Elmar Rueckert and Gerhard Neumann. A study of morphological computation by using probabilistic inference for motor planning. In *2nd international conference on morphological computation, Venice, Italy*, pages 51–53, 2011.
- [68] Thiago A Sarraf, Daniel S Marigold, and Stephen N Robinovitch. Maintaining standing balance by handrail grasping. *Gait & posture*, 39(1):258–64, jan 2014.
- [69] Christina Schmitz, Joëlle Martineau, Catherine Barthélémy, and Christine Assaiante. Motor control and children with autism: deficit of anticipatory function? *Neuroscience letters*, 348(1):17–20, 2003.
- [70] Stephen H Scott. Optimal feedback control and the neural basis of volitional motor control. *Nature Reviews Neuroscience*, 5(7):532–546, 2004.
- [71] Reza Shadmehr, Ferdinando A Mussa-Ivaldi, and Emilio Bizzi. Postural force fields of the human arm and their role in generating multijoint movements. *The Journal of neuroscience*, 13(1):45–62, 1993.

- [72] Harm Slijper and Mark Latash. The effects of instability and additional hand support on anticipatory postural adjustments in leg, trunk, and arm muscles during standing. *Experimental Brain Research*, 135(1):81–93, 2000.
- [73] Maurice A Smith, Ali Ghazizadeh, and Reza Shadmehr. Interacting adaptive processes with different timescales underlie short-term motor learning. *PLoS Biol*, 4(6):e179, 2006.
- [74] Paul J Stapley, Thierry Pozzo, Guy Cheron, and Alexander Grishin. Does the coordination between posture and movement during human whole-body reaching ensure center of mass stabilization? *Experimental Brain Research*, 129(1):134–146, 1999.
- [75] Doug Stewart. A platform with six degrees of freedom. *Proceedings of the institution of mechanical engineers*, 180(1):371–386, 1965.
- [76] T Sugihara and Y Nakamura. Whole-body cooperative balancing of humanoid robot using cog jacobian. In *IEEE/RSJ Int. Conf. Intelligent Robots and Systems*, pages 2575–2580, Lausanne, Switzerland, Oct 2002.
- [77] Tomomichi Sugihara and Yoshihiko Nakamura. Whole-body cooperative balancing of humanoid robot using cog jacobian. In *Intelligent Robots and Systems, 2002. IEEE/RSJ International Conference on*, volume 3, pages 2575–2580. IEEE, 2002.
- [78] Yuval Tassa, Tom Erez, and Emanuel Todorov. Synthesis and stabilization of complex behaviors through online trajectory optimization. In *Intelligent Robots and Systems (IROS), 2012 IEEE/RSJ International Conference on*, pages 4906–4913. IEEE, 2012.
- [79] Emanuel Todorov. Optimality principles in sensorimotor control. *Nature neuroscience*, 7(9):907–915, 2004.
- [80] Marc Toussaint, Nathan Ratliff, Jeannette Bohg, Ludovic Righetti, Peter Englert, and Stefan Schaal. Dual execution of optimized contact interaction trajectories. In *Intelligent Robots and Systems (IROS 2014), 2014 IEEE/RSJ International Conference on*, pages 47–54. IEEE, 2014.
- [81] Claes Von Hofsten. Prospective control: A basic aspect of action development. *Human development*, 36(5):253–270, 1993.
- [82] M Vukobratović and B Borovac. Zero-moment point – thirty five years of its life. *Int. J. Humanoid Robotics*, 1(1):157–173, 2004.
- [83] M Vukobratović, A Frank, and D Jurić. On the stability of biped locomotion. *IEEE Trans. Biomedical Engineering*, 17(1):25–26, Jan 1970.
- [84] L Žlajpah and J Babič. Body model 1.0 quick user manual. Technical report, Jožef Stefan Institute, Ljubljana, Slovenia, 2014.
- [85] Alan M Wing, Leif Johannsen, and Satoshi Endo. Light touch for balance: influence of a time-varying external driving signal. *Philosophical transactions of the Royal Society of London. Series B, Biological sciences*, 366(1581):3133–41, nov 2011.

- [86] D Winter. Human balance and posture control during standing and walking. *Gait and Posture*, 3(4):193–214, 1995.
- [87] David A Winter. Human balance and posture control during standing and walking. *Gait & posture*, 3(4):193–214, 1995.
- [88] Daniel M Wolpert and Zoubin Ghahramani. Computational principles of movement neuroscience. *nature neuroscience*, 3:1212–1217, 2000.
- [89] Daniel M Wolpert, Zoubin Ghahramani, and Michael I Jordan. Are arm trajectories planned in kinematic or dynamic coordinates? an adaptation study. *Experimental brain research*, 103(3):460–470, 1995.
- [90] T Yoshikawa. Dynamic manipulability of robot manipulators. *J. Robot Systems*, 2(1):113–124, 1985.